J. Fluid Mech. (1998), *vol.* 369, *pp.* 49–89. Printed in the United Kingdom

Development of a three-dimensional free shear layer

By A. J. RILEY† AND M. V. LOWSON

Department of Aerospace Engineering, University of Bristol, Bristol, BS8 1TR, UK

(Received 28 April 1997 and in revised form 9 March 1998)

Experiments have been undertaken to characterize the flow field over a delta wing, with an 85° sweep angle, at 12.5° incidence. Application of a laser Doppler anemometer has enabled detailed three-dimensional velocity data to be obtained within the free shear layer, revealing a system of steady co-rotating vortical structures. These sub-vortex structures are associated with low-momentum flow pockets in the separated vortex flow. The structures are found to be dependent on local Reynolds number, and undergo transition to turbulence. The structural features disappear as the sub-vortices are wrapped into the main vortex core. A local three-dimensional Kelvin–Helmholtz-type instability is suggested for the formation of these vortical structures in the free shear layer. This instability has parallels with the cross-flow instability that occurs in three-dimensional boundary layers. Velocity data at high Reynolds numbers have shown that the sub-vortical structures continue to form, consistent with flow visualization results over fighter aircraft at flight Reynolds numbers.

1. Introduction

There are both fundamental and practical reasons for an interest in the details of the development process in three-dimensional free shear layers. Free shear layers occur in many fluid problems such as jet flows, mixing layers and wakes. Curved three-dimensional free shear layers are widespread, being present over more complex geometries such as rearward facing steps, and flows with wall injection. In particular, complex separated vortical flow fields are also crucial to aerodynamic design of modern aircraft. On high-performance combat aircraft vortices occur over the slender forebody, the leading-edge extension (LEX) and the main wing, and dominate the aerodynamics of the aircraft at high angles of attack.

A delta wing flow field provides the most fundamental example of the basic separation features seen in most high angle of attack flows. At moderate angles of attack the pressure surface boundary layer on a delta wing is unable to negotiate the sharp leading edge and hence separates. The resulting free shear layers then roll up to form a pair of concentrated vortex cores over the suction side of the wing (figure 1), greatly enhancing the lift and improving the overall performance of the wing. Most detail studies of free shear layers have focused on situations where the free shear layer is essentially two-dimensional. Studies of three-dimensional shear layers have been less extensive, but have demonstrated that there are significant differences from the two-dimensional case. The slender delta wing at incidence provides the classic

† Present address: 45A Erpingham Road, Putney, London, SW15 1BQ, UK

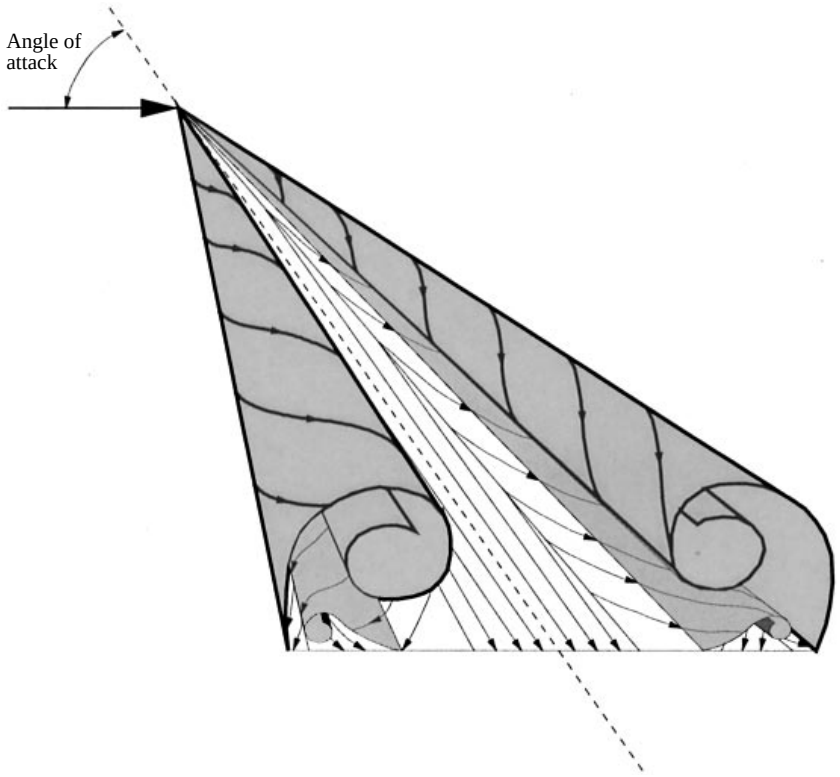

FIGURE 1. The vortical flow field over a delta wing at high angle of attack.

model flow for the examination of three-dimensional separated flows, and has been the subject of many studies, only some of which can be referenced here.

Perhaps surprisingly, relatively few of these studies have concentrated on the development of the shear layer itself. Most studies have been concerned with the nature and consequences of the rolled-up vortex core above the wing. This is found to exhibit many unexpected phenomena, for example vortex breakdown at higher angles of attack. The present work has concentrated on an examination of the development of the free shear layer as it leaves the leading edge and rolls up around the vortex cores. Phenomena associated with the major concentrated vortices are not examined in the present paper, other than as a by-product of the principal measurements.

It has been known for some time that the free shear layer on a delta wing is subject to a number of instability phenomena. The most obvious is a time-varying instability, closely related to the classic Kelvin–Helmholtz (K–H) instability of a two-dimensional free shear layer. This was first examined by Gad-el-Hak & Blackwelder (1985, 1986). It is generally found that this instability is shed uniformly along the leading edge of the wing, and then travels up and around the shear layer, finally to be wrapped into the core of the vortex. A key feature of this instability is that because it travels around the shear layer, it cannot be seen with the naked eye, and can only be observed through flash photography or equivalent techniques.

It was shown by Lowson (1988) that the K–H vortex structures formed in the shear layer on a delta wing went through a pairing mechanism, similar to that observed by Winant & Browand (1974) in a simple two-dimensional shear layer. It was also found that this unsteady instability was exceptionally sensitive to external

conditions. Travelling vortex structures could be generated from a wide variety of external sources, for example the vibration from the tunnel cooling fan operating at 50 Hz. Generally it has been found that phenomena associated with the travelling K–H instabilities in the strongly curved shear layer are essentially parallel to effects observed in a two-dimensional free shear layer. However, another form of shear layer instability has a variety of unexpected and, to date, incompletely examined features. These are steady instabilities, which can be readily observed with the naked eye, given some form of smoke or other visualization medium.

These structures within the rolled-up vortex core were examined in detail by Payne (1987), Payne *et al.* (1988) using both flow visualization and Pitot measurement techniques. The existence of significant steady sub-structure in the separated vortex flow was unexpected, and was initially thought to be related to the unsteady structures described above. However, Lowson (1988) conducted a survey over 70° and 80° delta wings at low Reynolds number in a wind tunnel which showed that the steady and unsteady instabilities were distinct, although there were significant mutual interference effects. It was shown that the steady instability could be observed close to the leading edge of the wing, where smoke visualizations showed a series of steady streaks in the separating shear layer. These amplified as the shear layer wrapped around the wing to develop into the larger scale steady structures originally observed by Payne. Reynolds & Abtahi (1989) confirmed these findings independently. They found both the steady and unsteady forms of instability over a 75° delta wing tested in a free surface water channel, and also showed that the steady longitudinal structures could be identified in the separating free shear layer at leading-edge sweeps of 56°. They again found that the unsteady instability was exceptionally sensitive to external disturbance, requiring a settling period of up to 30 minutes before the unsteady sources were not forced by residual disturbances in the water channel.

Campbell, Chambers & Rumsey (1989) presented preliminary flow visualization evidence suggesting that a steady instability structure of the turbulent shear layer also appeared at flight Reynolds numbers over the LEX of fighter aircraft. Condensation patterns could be seen under certain atmospheric conditions that had clear similarities to the low-speed laminar flow visualizations of Payne over slender delta wings. The existence of convected turbulent structures in a free shear layer at high Reynolds number is well known and is the topic of much debate, but the appearance of steady structures at full-scale Reynolds numbers is unexpected. More recent wind tunnel investigations over delta wings by Verhaagen, Meeder & Verhelst (1993) and Washburn & Visser (1994) have also found evidence of streamwise vortical structures at high Reynolds numbers (up to 1.25×10^6). Washburn & Visser used a five-hole Pitot static probe to locate the steady structures. This raises further questions, since it is well known that such measurements in the concentrated vortex core can be seriously misleading because the probe can induce vortex breakdown. Even though care was taken in these investigations to minimize the effect of the probe on the flow field, this was still an obvious concern given the small scale of the structures compared to the scale of measurement device. Washburn & Visser found that the streamwise sub-vortices were co-rotating, with vorticity the same sign as that of the shear layer, and followed helical streamlines into the core of the vortex. This was also found independently in a study reported by Lowson, Riley & Swales (1995) using laser Doppler anemometry.

The existence of steady vortical structures in a shear layer at high Reynolds number is significant for two reasons. First it suggests that the phenomena studied at low Reynolds number could have significant practical consequences. For example

there have been a series of major incidents, especially in the USA, associated with unexpectedly high levels of aerodynamic forcing on fighter aircraft at high angles of attack. Secondly, from the fundamental viewpoint, the continuity of phenomena from low to high Reynolds number suggests that the principal mechanisms may be inertial rather than viscous. The work reported in the present paper has been principally directed at obtaining a more detailed understanding of these steady structures.

There is also an interesting parallel with boundary layer flows. Two-dimensional instabilities, in particular the classic Tollmien–Schlicting waves, have been widely studied. However, it is now appreciated that many of the most critical phenomena in boundary layers are due to three-dimensional effects, cf. Saric & Reed (1988). Although transition, particularly in its early stages, can be described via two-dimensional models, the final stages of the transition process are normally dominated by three-dimensional instabilities. Many of the more important practical effects causing transition on real wings are also dominated by three-dimensional effects, including attachment line transition and cross-flow instabilities. Parallels with the free shear layer above may well be relevant. Whereas Tollmien–Schlicting waves travel with respect to the local flow, most of the more important three-dimensional instabilities (e.g. Taylor–Görtler or cross-flow) are characterized by steady longitudinal patterns, which can be readily visualized in experiment. Three-dimensional instabilities normally dominate boundary layer transition in practical circumstances.

The fact that the sub-vortices in the free shear layer instability are steady and co-rotating seems to be an important pointer to the potential mechanism. The most obvious feature of the flow is strong curvature, and it was initially suggested that the mechanism could parallel the Taylor–Görtler instability. However, as shown in the benchmark paper by Gregory, Stuart & Walker (1955) on the transition of a skewed boundary layer, the Taylor–Görtler form of instability has vortices of alternating sign, while cross-flow instabilities can generate co-rotating vortices. Thus there is a strong case for associating cross-flow instability with the source of the steady co-rotating sub-vortices in the free shear layer of a delta wing. This suggestion was first made by Washburn & Visser (1994). However, cross-flow instability is based on a mathematical proof of a simplified two-dimensional boundary layer. Free shear layer instability is normally dominated by K–H type instabilities, together with secondary three-dimensional effects, and hence should not be discounted.

Time-accurate unsteady numerical simulations of the Navier–Stokes equations by Gordnier & Visbal (1994, 1995) found a K–H type instability in the free shear layer of a 76° delta wing, although the formation of these unsteady vortices was not completely consistent with the experimental observations of Gad-el-Hak & Blackwelder or Lowson. Other computational investigations have also found unsteady flow behaviour in the leading-edge region over delta wings (Murman & Rizzi 1986; Verhaagen *et al.* 1995), but these solutions were not time-accurate and hence did not capture the unsteady vortical structures. However, neither these calculations, nor any other computational investigation to date, have shown any indication of a steady instability structure (see Visbal 1995, for a comprehensive review). This is of obvious concern, since an inability to reproduce a basic mechanism clearly identified at low Reynolds number calls into question the accuracy of more complex computations at high Reynolds number. There are clearly significant limitations with computational models of complex shear flows. Washburn & Visser suggest that the reason for the incorrect computational results is simply inadequate grid resolution. However, since the scale of the steady structures is generally the same as that of the unsteady structures successfully computed by Gordnier & Visbal, it seems that this explanation

must be incomplete. Reservations have also been put forward by Doligalski, Smith & Walker (1994) regarding the ability of numerical solutions of the Navier–Stokes equations, which employ fixed spatial meshes or spectral schemes, to accurately model the vortex-induced separation, and roll-up, of a viscous boundary layer. It was suggested that numerical computations adopting a Lagrangian type of specification would have more success, where trajectories of fluid particles are evaluated as functions of their initial position and time. This would be of benefit in modelling separation, since many fluid particles are convected into the region of separation, resulting in greater resolution. Separation of the windward boundary layer over a delta wing is usually fixed by a sharp leading edge. However, the primary vortex-induced separation of the leeward surface boundary layer that rolls up to form the secondary vortex is a process that, according to Doligalski *et al.* (1994), fixed spatial meshes and spectral schemes would find difficult to model. The presence of the secondary vortex is a key factor in the development of the free shear layer.

More recently, a Lagrangian-type numerical scheme has been successfully implemented on a uniformly accelerating flat plate by Koumoutsakos & Shiels (1996). The results established, for the first time, the presence of an intrinsic K–H instability structure in the free shear layers of a flat plate, confirming previous experimental evidence, such as the clear visualizations of Pierce (1961). These computational results manage to reproduce the structure of previous experimental visualizations with far more success than that of the Eulerian schemes used to model the K–H instabilities found over delta wings. There are certainly parallels here between the two-dimensional case of a flat plate and the three-dimensional development over a delta wing, as previously mentioned by Lowson (1988). However, application of Lagrangian schemes to the delta wing problem is an avenue of research that is yet to be explored. As will always be the case, there is still a need for detailed accurate experimental data not only to validate present-day computational models, but also to provide a basis for the formulation of new and more accurate models.

2. Present experiments

2.1. *Background*

The present experiments build from previous investigations which used flow visualization to study the development of the shear layer and the formation of both the unsteady and steady instabilities (Lowson 1988, 1991). The earlier experiments were undertaken at low Reynolds number over a 70° and an 80° sweep delta wing. This research was hampered by the difficulty in obtaining useful flow field measurements at low air speed with conventional instrumentation, and also by a degree of flow unsteadiness, again as a direct result of the low air speed.

It was found that transition effects were usefully delayed by increasing the sweep angle of the wing, and the present research has been conducted on 85° delta wings. On these wings transition is delayed to such an extent that higher air speeds, ranging from 3 to 10 $\mathrm{m\,s^{-1}}$, can be used to study the laminar instability flow mechanisms. This is an attractive speed for the use of modern laser Doppler anemometry (LDA) for three-dimensional flow measurement.

The results presented in this report depend on new methods for high-resolution LDA measurements, which have recently been developed at the University of Bristol (Swales *et al.* 1993). One of the principal benefits of this enhanced resolution lies in the minimization of the error incurred within regions of steep velocity gradient.

Λ	c	t	t/c	σ
85°,[a]	471	11.5	0.024	30°
85°	435	3.3	0.008	45°
85°	444	1.3	0.003	30°

TABLE 1. Geometrical details of the three 85° delta wings used in these experiments – all linear dimensions in mm (a – plenum chamber).

This has enabled highly accurate measurements to be made throughout the complex flows found over delta wings at these low Reynolds numbers. In previous experiments in air it was often found that useful data could not be obtained over a region of concentrated vorticity. This was due to the poor signal to noise ratio of the LDA techniques employed. New techniques developed within the Department of Aerospace Engineering, University of Bristol (and described in more detail in § 2.4) have provided a method for overcoming the shortcomings experienced by previous investigators. The availability of these techniques was an important element in the planning of the present work.

2.2. *Model and wind tunnel*

The experiments were conducted in the 0.8m×0.6m low-turbulence, closed-return wind tunnel in the Department of Aerospace Engineering. The tunnel has a contraction ratio of 12 : 1, and was specifically designed to produce a turbulence level of less than 0.05% over the full working range of the tunnel (1–100 m s^{-1}). In previous work, Lowson (1988), a high-blockage peg board had been inserted immediately downstream of the working section in order to allow the tunnel velocity to be reduced to 0.09 m s^{-1}, whilst retaining low turbulence. In the present experiments the peg board has not been used while taking velocity data, although some references will be made to the type of flow field obtained under those conditions. The cooling fan for the wind tunnel motor that imparts an unwanted 50 Hz vibrational input to the model was disengaged for the present experiments.

The 85° delta wing in this survey was manufactured to a high degree of precision. The surface roughness on the wing was measured at 1.5 μm. The leading edge of the wing was made as thin as possible and averaged 0.12 mm in thickness. The wing was constructed containing a plenum chamber and a uniformly machined smoke slot, 0.2 mm wide and situated 1 mm below the leading edge of the wing. This permitted smoke to be released directly into the shear layer at the wing leading edge. A direct comparison between velocity data and flow visualization results was possible. The plenum chamber extended from $x/c = 0.26to1.0$ (non-dimensionalized chordlength, origin at the apex of the wing), and thus could not provide flow visualizations close to the apex of the model. Two further 85° wings, without plenum chambers, were also used to study the effect of windward geometry on the shear layer instabilities. The dimensions of the wings are shown in table 1. The geometrical terms, together with the body-fixed axis system being used, are defined in figure 2.

The support rig was based on a two-strut system which incorporated a turntable to allow full variation in the angle of yaw. The silver steel struts were both 12 mm in diameter and attached to the wing via simple brackets. The brackets were located at $x/c = 0.7$ and $x/c = 0.95$, on the non-chamfered section of the pressure surface. The pipe inlet to the plenum chamber was located at $x/c = 0.8$, in between the two struts. The incidence for these tests did not need to be determined from outside the

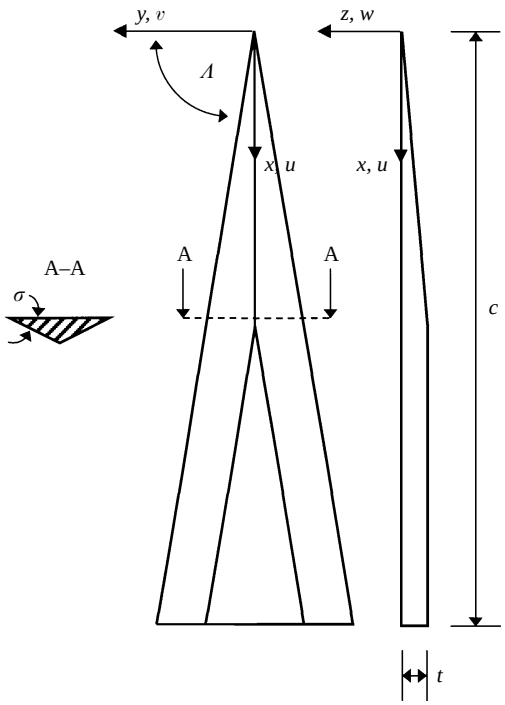

FIGURE 2. Schematic of the delta wing defining the geometric parameters in table 1.

tunnel. Hence the largest error in the measured incidence was the degree to which one-dimensional flow could be achieved in the test section. This could be guaranteed to $\pm 0.03^\circ$. All the major results reported in the present paper were taken at a single angle of incidence (α) of 12.5°.

2.3. *Flow visualization*

A Spectra–Physics 5 W argon-ion laser, operating in all lines mode, was used to illuminate the flow by creating a light sheet via a small cylindrical lens. An optical bench set-up provided beam steering to achieve a light sheet of specific height and chordwise position. The cylindrical lens could then be rotated to position this light sheet at any prescribed angle of incidence in the tunnel. For the cross-sectional visualizations of the flow field it was inclined normal to the wing surface.

The principal flow visualization medium used was smoke, which was generated by vaporizing mineral-based oil on a heated metal filament. The smoke was then injected into the plenum chamber within the wing and released through the leading-edge slots. The smoke was injected under minimal pressure to avoid disturbing the windward boundary layer, which defines part of the initial conditions for the free shear layer. There was some concern over the possible effects of the leading-edge smoke slot on the flow data acquired. Velocity data were acquired over the wing both with smoke visualization and with the slot blocked. There was no discernible difference in the results and hence the method of introducing the visualization medium into the flow field was validated.

The flow visualization photographs presented have been illuminated using either a laser light sheet or a flash, and in some cases both. A 35 mm camera with motor drive was used together with Kodak T-Max film (400 ASA). For the laser light sheet,

which presents a cross-section of the flow field, photographs were taken at a minimum exposure of 1/2000 s at f1.2 in order to capture an instantaneous picture. The flash photographs, which illuminated the whole flow field, were taken at 1/125 s at f22. The longer exposure was, in fact, the shortest exposure that could be synchronized with the flash. However, since the time that the flow field was illuminated depended upon the speed of the flash, which is approximately 1/10 000 s, the longer exposure did not affect the sharpness of the picture. The small aperture was required to provide sufficient depth of field to bring the whole flow field into focus. The combination of both laser light sheet and flash required a longer exposure than for the flash photographs and in the cases shown 1/15 s was used. This was due to the small aperture, required to provide adequate depth of field, not providing enough light to capture the laser light sheet.

2.4. *Laser Doppler anemometer*

2.4.1. *LDA apparatus*

Low wind tunnel speeds are necessary to observe the free shear layer structure in the laminar regime over a delta wing. The flow field under these conditions has been found to be highly sensitive to both external noise input and also probe interference. The non-intrusive aspect of the LDA technique was essential for obtaining useful flow field measurements.

The Dantec three-component LDA employed consists of two optic heads mounted on a fully automated three-axis traverse mechanism. The optic heads are linked by means of two 10 m long fibre-optic cables to a Spectra–Physics 5 W argon-ion laser. Both optic heads are free to be rotated within their respective gimbal mounts, which, in turn, can be swept and dipped to provide the required optical configuration. Two pairs of beams (green and blue) are emitted from one head, referred to as the '2D' head, and a third violet pair from the opposing '1D' head. Both heads are able to receive as well as transmit light and consequently either the direct backscatter (receiving light from the same head) or the off-axis backscatter (receiving light from the opposing head) mode of light collection can be employed. The raw data collected by the LDA is in terms of the frequency of the Doppler burst signals generated by seeding particles, measured in three non-orthogonal components. In the present experiments the seeding particles were produced by two Dantec Type 55L18 atomizers (Ondina oil based), which resulted in an average particle size of 0.7 μm. The frequency information for each channel is then processed by means of three Dantec Burst Spectrum Analysers.

2.4.2. *LDA alignment*

Each time the LDA was set up outside the tunnel it was necessary to obtain an optical configuration that would allow the measurement volume to reach the appropriate parts of the flow field. This, obviously, can change depending on the model being used, the angle of attack and the region of the flow required to be measured. Once the optical configuration has been decided upon, the beams and the collection volumes need to be brought to a common focus. The technique, described in detail by Swales *et al.* (1993), consists of employing the output of a light-dependent resistor mounted behind a 20 micron pin-hole to determine the peak intensity position (assuming a quasi-Gaussian distribution) across either a beam or a collection volume. By bringing the foci of the two collection volumes, and then each of the six beams in turn, to the face of this pin-hole a very high level of alignment can be guaranteed. The principal advantage of the technique is that it does not rely on the visual

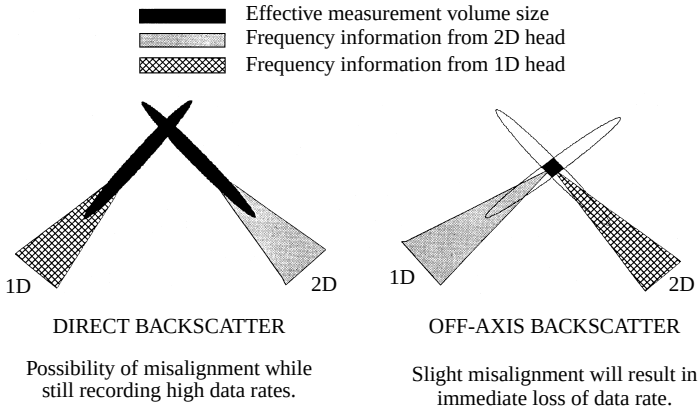

FIGURE 3. The two different modes of light collection, illustrating the much smaller measurement volume obtainable with the off-axis backscatter mode of light collection.

interpretation of the images of beams passing through an objective lens, but rather on the quantitative output of a meter.

Alignment has been found to be the absolutely crucial factor in obtaining good data. With good alignment higher data rates can be consistently guaranteed and, most importantly for this application, the simultaneous, off-axis backscatter mode of light collection can be employed. In this mode, light scattered by particles crossing the intersection volume created by the beams from one head, is received by the opposing head. This differs from the direct backscatter mode where the collection volumes are aligned with their respective intersection volumes (figure 3). The resultant measurement volume is consequently more spherical, rather than the classical, ellipsoidal shape as defined by the e^{-2} law, Drain (1980). In terms of the transit time, that is the time for which the Doppler signal is validated, an effective spherical measurement volume of less than 0.1 mm in diameter can be guaranteed. Furthermore, if hardware and software coincidence filtering is employed, then a burst is only accepted if a seeding particle passes through all three effective measurement volumes simultaneously. This results in a further reduction in the measurement volume size. The average size of the measurement volume, based on the transit distance for a typical coincident data set, was found to be 0.048 mm. Resolutions of 0.050 mm can be regularly attained using this technique. This level of resolution was critical to obtaining the data presented herein.

Many attempts to use LDA techniques to measure velocities in the vortex core in air have failed due to the centrifuging effect, which tends to remove particles from this region. In the direct backscatter mode of light collection it is far easier to obtain a good alignment which, together with the significantly elongated size of the measurement volume, guarantees high data rates. This has led to investigators using the direct backscatter mode of light collection in order to increase the data rate in the vortex core. However, the measurement volume can be up to 3 mm in length in this mode of light collection and will result in a significant velocity biasing, unless the model and the wind tunnel are large enough for this length scale to be insignificant. The flow field structures being studied in this experimental set-up are of the same order of magnitude as the length of the direct backscatter measurement volume, hence it is necessary to employ an off-axis configuration. Furthermore, there is no guarantee

that the two optic heads are recording data from the same spatial position in the direct backscatter mode, due to the fact that they are operating independently.

Velocity biasing can also be accentuated by the variation in the seeding density found across vortex flows over delta wings in air. This is characterized, as mentioned above, by the lack of particles found in the vortex core. The consequences of velocity biasing due to seeding density are similar to biasing due to velocity gradients. A greater number of signals are detected from the region of flow more densely seeded within a measurement volume, mirroring the case of more signals being detected by the region of higher speed flow within a measurement volume. The elongation of the measurement volume using a traditional direct backscatter approach, together with this variation in seeding density, has meant that data are swamped by extraneous signals along the length of the measurement volume. It may be noted that although the seeding density issue would not be a problem in water-based measurements, the other issues discussed would apply equally.

The high resolution gained by operating in the off-axis backscatter mode of light collection has been made workable by increased data rates, due to the accuracy of the new alignment techniques. This eliminates the problems of previous direct backscatter-based LDA techniques and provides a capability for effective measurement throughout the whole vortical flow field.

2.5. *Data reduction and presentation*

It is necessary to convert the frequency data obtained by the LDA to velocity data using calibration factors, which are based on the wavelength of the light in the particular pair of beams being considered and on the semi-angle of the beam separations. The three non-orthogonal velocity vectors are then transformed into a global set of orthogonal velocity vectors (u, v, w). The matrix for this transformation was calculated using the pin-hole meter and the LDA traverse system (Rickards, Swales & Barrett 1995). Using the pin-hole it is possible to determine coordinate locations for all six beams in two planes perpendicular to the y-axis of the wing. From these coordinates beam vectors can be calculated which allow the determination of the beam separation angles and the beam measurement vectors, the former providing accurate calibration factors and the latter leading to the transformation matrix. The ability to determine the accuracy of the location of the beam centres, using the traverse and the pin-hole meter, has enabled an estimate of the error associated with the complete transformation from non-orthogonal frequency data to orthogonal velocity vectors. This has been reported in Riley (1996), together with an estimation of other possible errors in the system. For the data presented in the present paper the largest error in the measured velocities is due to the matrix transformation from non-orthogonal frequency data to orthogonal velocity vectors and is equal to $\pm 1.8\%$ of the total velocity magnitude.

The velocity data have been presented in terms of the body-fixed axis system defined in figure 2. The term 'axial' has been used throughout this report to define the x-axis direction, in the same way that 'spanwise' and 'vertical' have been used to represent the y-axis and the z-axis directions, respectively. The requirements of these tests were for traverses to be performed perpendicular to the upper surface of the delta wing in a spanwise direction. The development of the instabilities was determined, from flow visualization, to be the same for both sides of the wing. Hence, a more detailed grid could be specified, for a given number of data points, by considering only the starboard side of the delta wing. The data grid density has been specified in the figure captions of all the velocity and vorticity contour plots in terms of the grid spacing

$(\Delta y, \Delta z)$. The two-dimensional grids used have been of a constant density in both axis directions and hence only one dimension is given, e.g. $\Delta(y, z) = 1$ mm.

The origin of the y-coordinate in the velocity and vorticity contour plots is not related to the body-fixed axis system. However, the z-coordinate needs to be defined relative to the surface of the wing. For the results in § 3.2, § 3.3 and § 4.2 the z-coordinate origin is approximately 1 mm off the wing surface. The surface of the wing has been defined schematically in § 4.1 and for the free shear layer profiles in § 4.3 the origin is coincident with the wing surface.

The axial vorticity (ω_x) is represented by the gradients of the in-plane velocity vectors (v, w) and has been calculated using a central difference method to obtain the velocity gradients

$$\omega_x = \frac{\partial w}{\partial y} - \frac{\partial v}{\partial z}. \tag{2.1}$$

The vorticity vector is defined as being positive in an anti-clockwise direction looking in a positive direction along an axis. The majority of the data have been obtained on the starboard vortex, hence the axial vorticity vector of the primary vortex will be negative based on the axes convention above. The circulation (Γ) has been obtained by taking the line integral of the velocity ($\boldsymbol{u}$) around a specified area, where $\boldsymbol{l}$ is the unit line vector

$$\Gamma = \oint \boldsymbol{u} \cdot \mathrm{d}\boldsymbol{l}. \tag{2.2}$$

Both the vorticity and the circulation have been non-dimensionalised in all cases by the free-stream velocity (U_∞) and the wing chordlength (c).

3. Results: the development of the flow field

3.1. *Flow field visualizations*

Figure 4 shows the basic development of the flow field over the wing as a function of Reynolds number (i.e. tunnel velocity) using the wing with the plenum chamber. The photographs show the overall flow field taken from outside the tunnel together with a simultaneous section through the vortex structure taken at 0.6 chord using the laser light sheet. Over the chord length of the wing, at a specific Reynolds number, it is possible to observe laminar, transitional, and turbulent flow. It can also be seen that, although the flow processes are complicated, they do follow a systematic development with increase in Reynolds number.

At Reynolds numbers based on chordlength (Re_c) of less than 3×10^4 the shear layer showed no sign of any instability structure or periodic activity and followed a cylindrical/helical spiral around and into the core of the primary vortex. The very lowest Reynolds numbers required low tunnel speeds which were obtained through the use of the peg-board. Figure 4 (a) shows the flow field at $Re_c = 4.19 \times 10^4$, the lowest full-chord Reynolds number achievable without the presence of the peg-board, where it can be seen that streamwise structure has just begun to appear near the trailing edge. The cross-sectional views at $x/c = 0.6$ correspond to a laminar flow. The results at these low Reynolds numbers were consistent with the results previously obtained by Lowson (1988) on less slender delta wings. The separated flow is dominated by the effects of viscosity, and the patterns observed, particularly towards the centre of the vortex, represent streak lines in a laminar flow rather than any well defined shear layer. It may be noted that the observed spiral results from smoke inserted at the leading edges

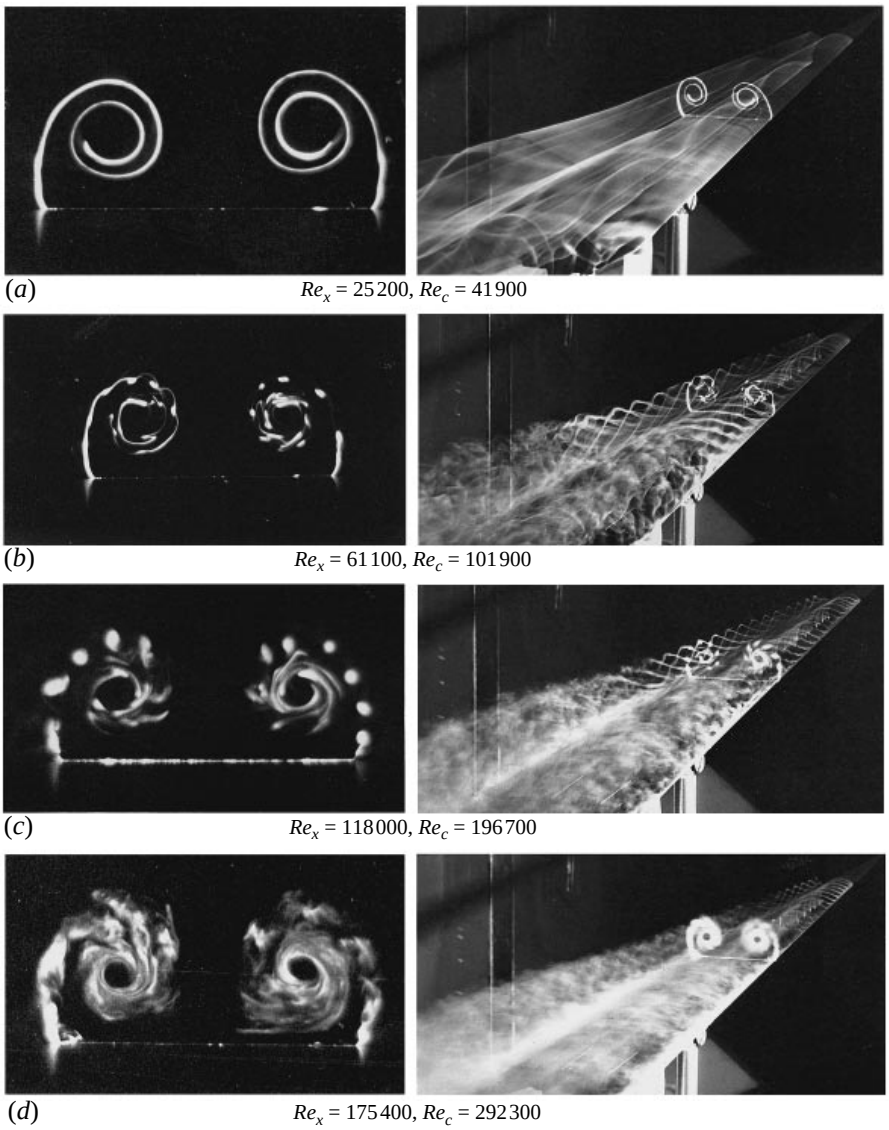

FIGURE 4. Cross-sectional views ($x/c = 0.6$) and combination of full and cross-sectional views of the flow field over the 85° delta: $\alpha = 12.5°$.

progressively more upstream. The termination of the visualization trace after about two turns is because smoke has not been introduced further upstream than 0.26 chord.

As the Reynolds number increases beyond 4×10^4 the streamwise structures become far more distinct, and form progressively further upstream towards the apex of the wing. The smoke filaments can be seen to form near the leading edge of the wing and spiral into the core of the vortex as they pass downstream. As the Reynolds number is increased still further an unsteady flow can be seen at the trailing edge, masking any structure to be found in the shear layer and representing the transition to turbulence (figure 4 *b*). Comparing the cross-sectional visualizations of figure 4 (*b*) and figure 4 (*c*) it can be seen that the streamwise structures themselves become more distinct with increasing Reynolds number. Figure 4 (*d*) shows a case for which the

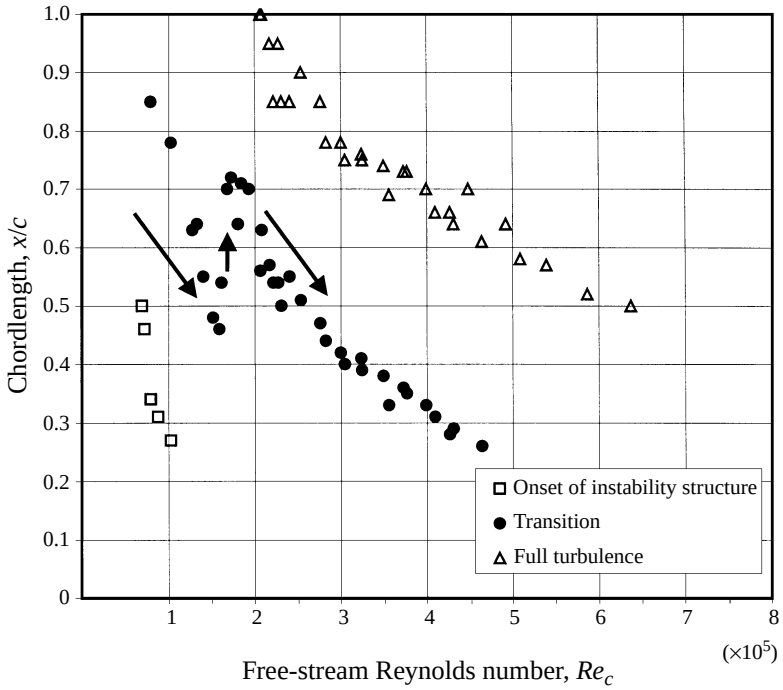

FIGURE 5. Chordwise location of various flow features with increasing Reynolds number. Progression of the unsteady flow has been indicated by arrows: $\alpha = 12.5°$.

flow has become turbulent at 0.6 chord, radically changing the appearance of the laser light sheet section. With further increase in Reynolds number the unsteady flow continues to move towards the apex of the wing until the whole separated flow field is turbulent beyond $x/c = 0.26$, the point at which smoke is released into the flow.

Analysis of the flow field was undertaken using a laser light sheet to correlate the onset of the shear layer structure, transition and full turbulence with increasing Reynolds number. The results are shown in figure 5 in terms of the free-stream Reynolds number and non-dimensional chord length. Transition was defined as the chord location where unsteadiness could first be observed in the flow field. Turbulence represented the condition under which there was no visible laminar structure left throughout the whole of the local flow. These definitions rely on subjective interpretation, but in practice it was found that the chord locations for the appearance of each phase of the process could be defined with good accuracy. Repeat estimates of chord location were usually within 2%. The chordwise position of transition was generally found to be inversely proportional to the free-stream Reynolds number. However, there was a clear discontinuity in the upstream progression of transition, which can be observed in the data of figure 5.

At $Re_c \approx 0.70 \times 10^5$ disturbances appeared at the trailing edge of the wing, gradually moving upstream with increasing Reynolds number, and were at first assumed to represent a natural transition to turbulence. However, at $Re_c \approx 1.60 \times 10^5$ the disturbances moved rapidly back downstream. It was established through photographic evidence that at $Re_c < 1.60 \times 10^5$ the unsteadiness corresponded to a K–H-type instability structure, as can be seen in the flash photographs of figure 6. This can be identified as congregations of smoke particles forming at the leading

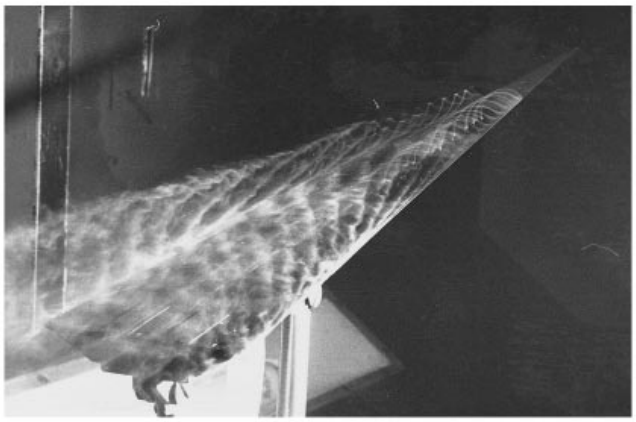

FIGURE 6. The appearance of the unsteady instability in the free shear layer: $\alpha = 12.5°$; $Re_c = 164\,900$.

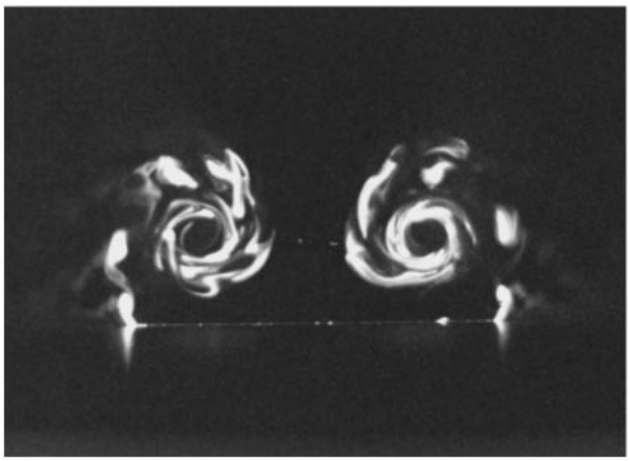

FIGURE 7. Cross-sectional view of the unsteady instability showing how the structures are stretched as they are wrapped into the vortex core: $\alpha = 12.5°$; $x/c = 0.6$; $Re_c = 164\,900$.

edge and travelling with the shear layer around the vortex. As mentioned above, in the experiments of Lowson (1988) it was found that this instability could occur prior to the steady streamwise instability, and would interact with the steady instability to cause premature transition. Figure 7, a cross-sectional view, clearly shows the K–H vortical structures being wrapped into the core flow. Comparison with the laser illuminated cross-sections in figure 4(*c*) show a significant change in the type of vortical structure formed at the leading edge. It should be noted that figure 7 was captured with a shutter speed of 1/2000th s, and that these structures were not visible to the naked eye. This form of disturbance is characteristic of previous observations of the K–H instability. Beyond $Re_c \approx 1.60 \times 10^5$ the steady sub-structure re-forms back down the wing and the K–H instability is no longer prominent (figure 4*c*). The fact that, at higher Reynolds numbers, the shear layer re-forms back into the steady streamwise structures suggests that the unsteadiness associated with the K–H instability was not a fundamental part of the transition to turbulence. The appearance of the K–H instability was found to be dependent upon a certain range of tunnel

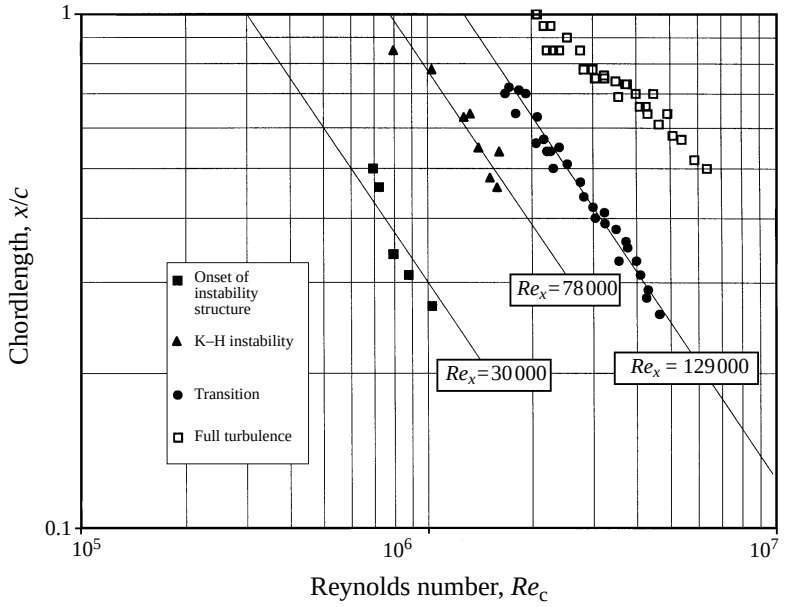

FIGURE 8. Chordwise location of the flow features with increasing Reynolds number plotted on a log-log scale: $\alpha = 12.5°$.

velocities. It will be recalled that although several previous investigators have reported the generation of K–H instabilities under force-free conditions, it has also been found that the flow is highly sensitive to external disturbance. These external disturbances can actually initiate the formation of unsteady vortices, when none are present under force-free conditions (Reynolds & Abtahi 1989). Due to the above evidence, it is assumed that this feature of the present results is due to extraneous inputs and should be discounted as a generic part of the flow. Figure 4 (*c*) again shows a region of unsteady flow downstream of the streamwise structure. However, there is no sign of the characteristic K–H structure and it was assumed that this represented a turbulent flow field.

The chordwise data are replotted on a log scale in figure 8. The transition, the initial formation of the K–H instability and the onset of the steady instability all collapsed into straight lines indicating a clear dependence on a local chord Reynolds number. The lines shown in figure 8 correspond to local Reynolds numbers (Re_x) based on distance from the apex of 129 000, 78 000 and 30 000, respectively. The fact that the chordwise position of the K–H instability was dependent on a local Reynolds number, in the range of tunnel velocities for which it was present, was unusual considering previous investigations had found the formation to occur simultaneously along the whole of the leading edge. Figure 7 clearly shows that the formation of the K–H instability is limited to a certain region along the chordlength. The turbulent data, although fairly subjective in their definition, give a clear trend for chord location of fully turbulent flow as a function of Reynolds number. Referring back to figure 5 it can be seen that the length of the transition region, from the start to the location of full turbulence, is essentially constant and equal to about 0.35 chord. Thus the final appearance of turbulence does not a obey a simple inverse law with Reynolds number. (For reference the data are matched by the curve $x/c = 1052 Re_c^{-0.57}$.) For the

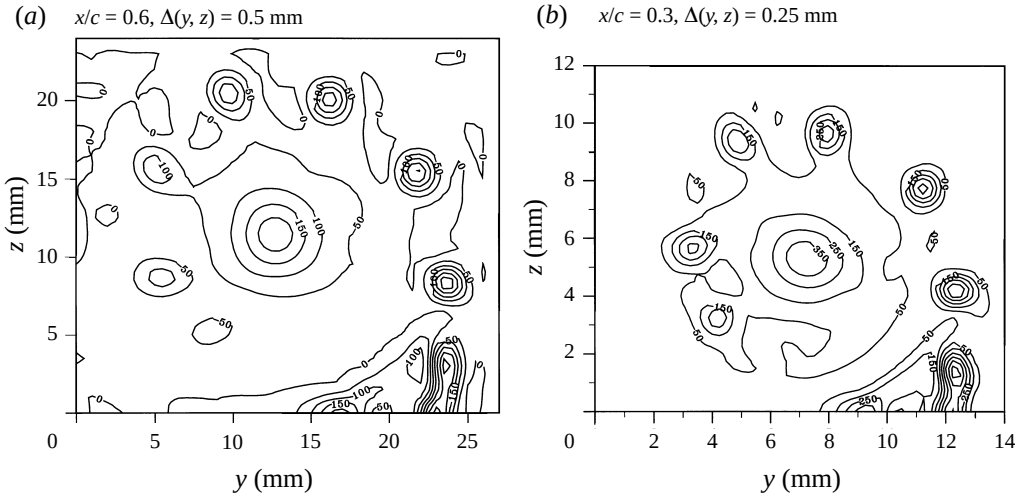

FIGURE 9. Comparison of the axial vorticity distribution at two different chordwise stations, at the same local Reynolds number: $\alpha = 14°$; $Re_x = 112\,600$.

other effects the dependence on local Reynolds number is unsurprising, particularly since this is a conical flow.

One point which is obvious from the visualizations, but which needs to be borne in mind during interpretation of the results, is that locations around the spiral from the leading edge are associated with flow at the leading edge at progressively more upstream locations. Thus the flow in the cross-flow plane close to the leading edge has arisen from locations just upstream, while further around the spiral the flows observed, for example the concentrated vortex structures, have been generated some distance upstream and have had an opportunity to develop during their passage down the wing. However, it can be seen from the visualizations that any development in the steady structure (apart from transition) is relatively small.

3.2. *Laser Doppler measurements of the flow field*

The whole process described above from visualization studies was further analysed using the LDA. Because the key flow processes of interest are steady, data on the flow field can be captured by traverses. This does require that the tunnel speed is carefully controlled to be constant. Any unsteadiness in the flow would appear as false spatial variations in the data recorded. This potential problem was kept in mind throughout the work, and few data had to be discarded because of non-stationary measurement conditions. It is believed that overall accuracy of the data reported is as projected from analysis of the LDA error process (cf. § 2.5).

The local Reynolds number was varied both by taking velocity data at a fixed chord position ($x/c = 0.6$) and gradually increasing the tunnel velocity, and also by taking velocity data at different stations down the wing at a constant tunnel velocity. Results from these two approaches tended to confirm the conclusions from the flow visualizations, regarding local Reynolds number dependence of the flow field. Figure 9 compares the axial vorticity derived at stations 0.3 and 0.6 chord, at tunnel velocities such that the local Reynolds number is the same. It can be observed that the whole structure of the flow is essentially identical. The (non-dimensional) position and size of the sub-vortices, and (to slightly less accuracy) the vorticity/velocity contours, are very closely correlated in the two cases. Note that the contour spacing in figure 9 (*a*) is

half that in figure 9 (*b*) and that the reduction in the core vorticity is due to diffusion effects as the scale of the flow increases downstream. Similar results have been found for all other equivalent cases examined.

Figure 10 (*a–f*) shows plots of the axial vorticity for a steadily increasing local Reynolds number at a fixed chord position of $x/c = 0.6$, in the range $Re_x = 0.74 \times 10^5 - 1.70 \times 10^5$. This is the local Reynolds number range over which the streamwise structure develops and the transition to turbulence occurs. The distribution of the axial vorticity in these two-dimensional grids shows that the congregation of smoke particles into streamwise streaks corresponds to steady vortical structures, all rotating in the same sense as the main vortex. It can be seen that the wavelength of the vortices decreases only slightly throughout the range of Reynolds number shown; however the strength and the shape changes considerably. The circulation within the sub-vortices that form at the leading edge increases as the local Reynolds number increases, prior to transition. Also the shape of the vortices becomes more circular as the local Reynolds number increases. The appearance of the K–H instability masks the streamwise structure for the range $Re_x = 0.78 \times 10^5 - 1.03 \times 10^5$ corresponding to the trends defined in figure 8. Figure 10 (*b*) corresponds to data taken in this range and the apparent weakening of the vortical structures measured is thought to be an artefact of the unsteady flows due to the K–H instability at those tunnel speeds.

Figure 11 presents the vorticity distribution across the whole of the wing at $Re_x = 1.18 \times 10^5$. The colour shading gives a far better indication of the variation in positive and negative vorticity between the secondary vortices, the sub-vortices and the primary vortices. The development of the port vortex can be seen to lag the starboard vortex (see figure 10 *c, d*). It was possible to obtain a symmetrical flow field through careful on-line adjustment of the yaw angle, using flow visualization to ascertain the symmetry of the flow field. The flow field was highly sensitive to the yaw angle, small variations of less than $\pm 0.5^\circ$ having a significant effect.

The wavelength (λ) of the vortical structures was calculated, from both flow visualization and axial vorticity distributions, by taking the average in-plane distance between the centres of at least five of the sub-vortices. The measurement accuracy of the wavelength was found to be approximately $\pm 2\%$. The wavelength is non-dimensionalized by the local chordlength and plotted against the local Reynolds number in figure 12, at two different chord stations, $x/c = 0.6$ and $x/c = 0.8$. The data collapse reasonably well based on the local chordlength and can be seen to decrease slightly as the local Reynolds number increases. This is despite a general increase in the scale of the sub-vortex structures with increase in Reynolds number. The gap in the data at $x/c = 0.6$ is due to the appearance of the K–H instability. By analysing the flow field at $x/c = 0.8$ it was possible to obtain wavelengths at local Reynolds numbers in this 'gap' region, prior to the K–H instability regime that was dependent on the tunnel velocity. It does appear that the non-dimensional wavelength of the sub-vortices decreases as the local chord station increases. However, more data would be required to confirm this point. Data taken at other angles of attack or sweep in the present experiments confirmed the results from other experiments e.g. Lowson (1988), Washburn & Visser (1994), showing that the size and wavelength of the sub-vortices are reduced by an increase in either angle of attack or sweep.

The axial velocity distribution also shows the structure of the shear layer as shown in figure 13 (*a*). At the lowest Reynolds number the axial velocity in the sub-vortices is little different to the main flow. At such speeds the axial velocity in the main vortex core is also close to that of the main stream. However, as the Reynolds number increases the axial velocity in the sub-vortices reduces compared to the immediately

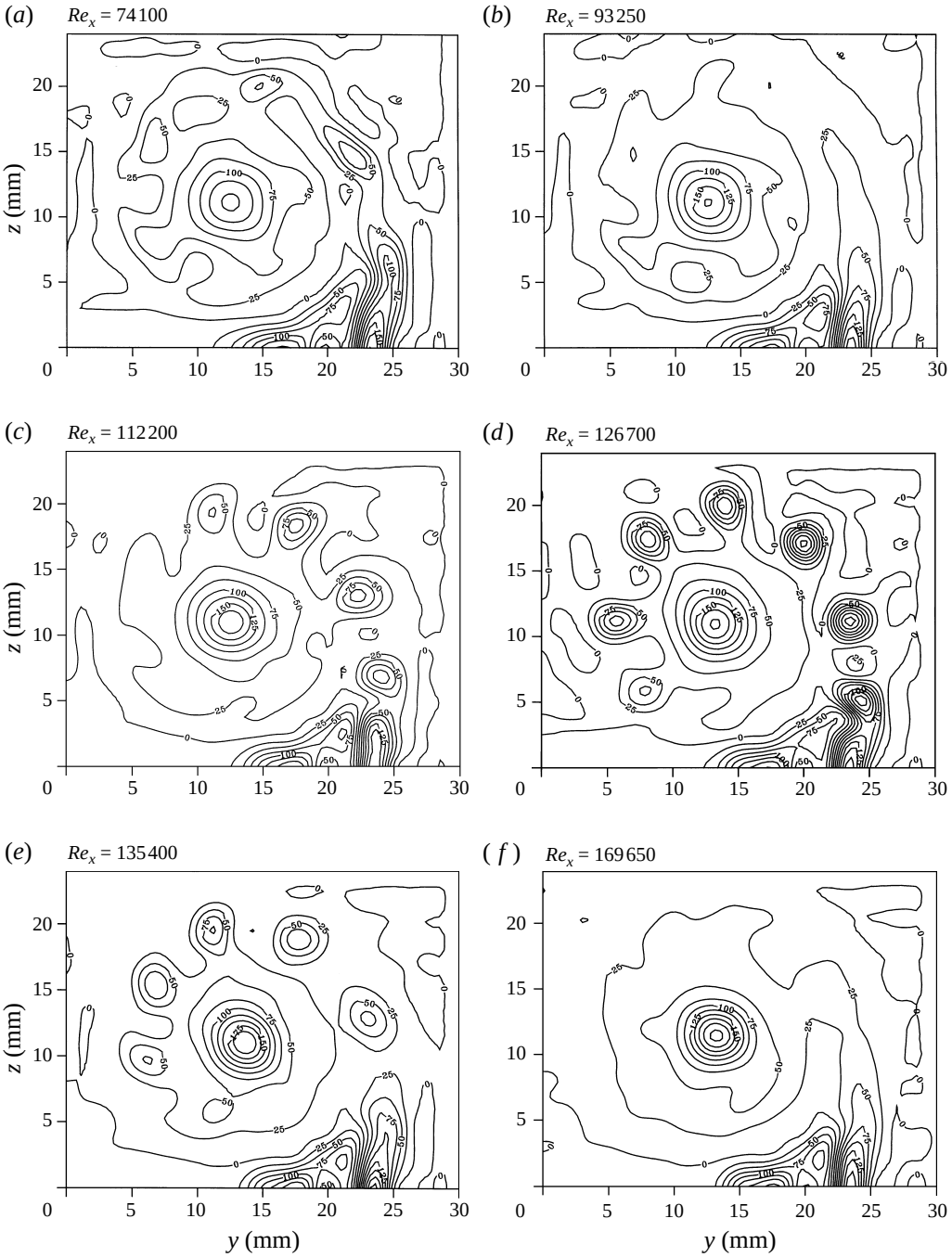

FIGURE 10. Variation in the axial vorticity due to an increase in local Reynolds number. The local Reynolds number was varied by increasing the tunnel velocity: $\alpha = 12.5°$; $x/c = 0.6$; $\Delta(y, z) = 0.75$ mm.

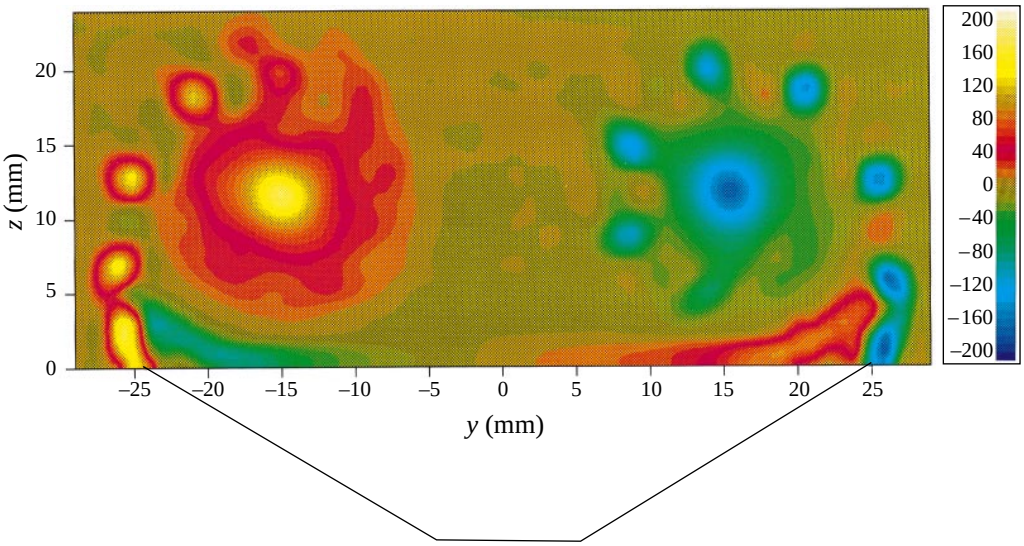

FIGURE 11. Variation in the axial vorticity across the whole of the leeward surface, together with the cross-section of the wing: $\alpha = 12.5°$; $x/c = 0.6$; $Re_x = 118000$; $\Delta(y, z) = 1$ mm.

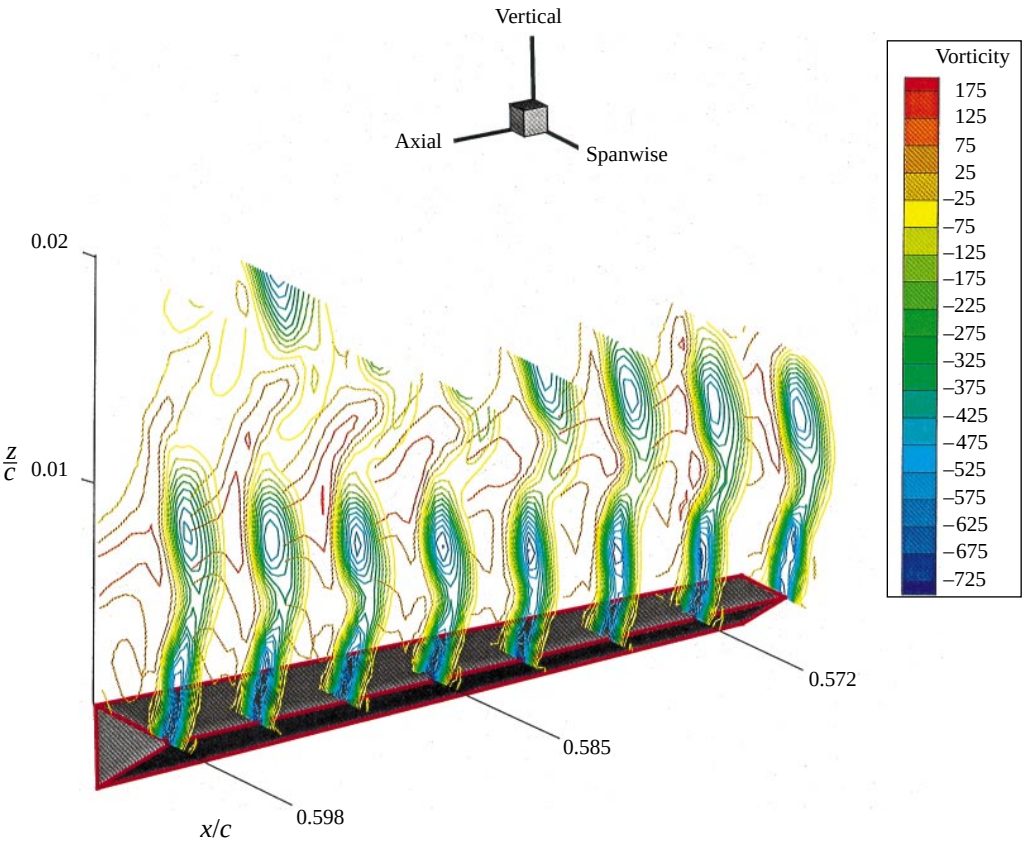

FIGURE 25. Three-dimensional axial vorticity data set showing the formation of a sub-vortex at the leading edge of the wing: $\alpha = 12.5°$; $Re_c = 174\,300$; $\Delta(y, z) = 0.25$ mm.

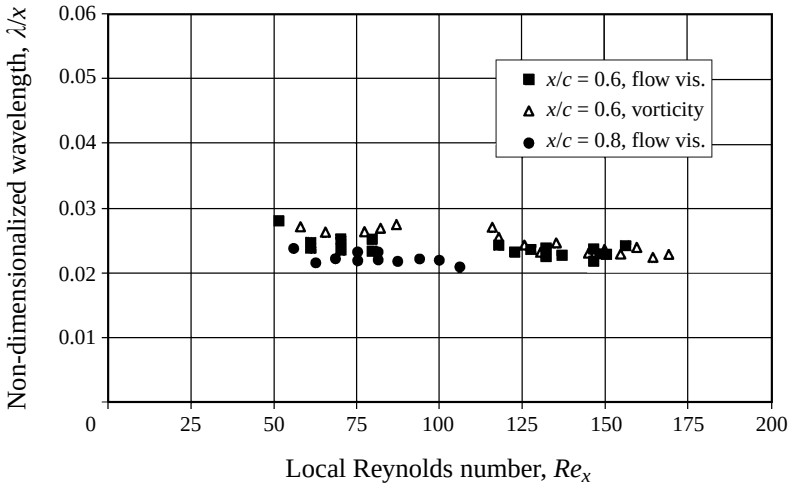

FIGURE 12. Variation in the wavelength of the vortices with increasing local Reynolds number: $\alpha = 12.5°$.

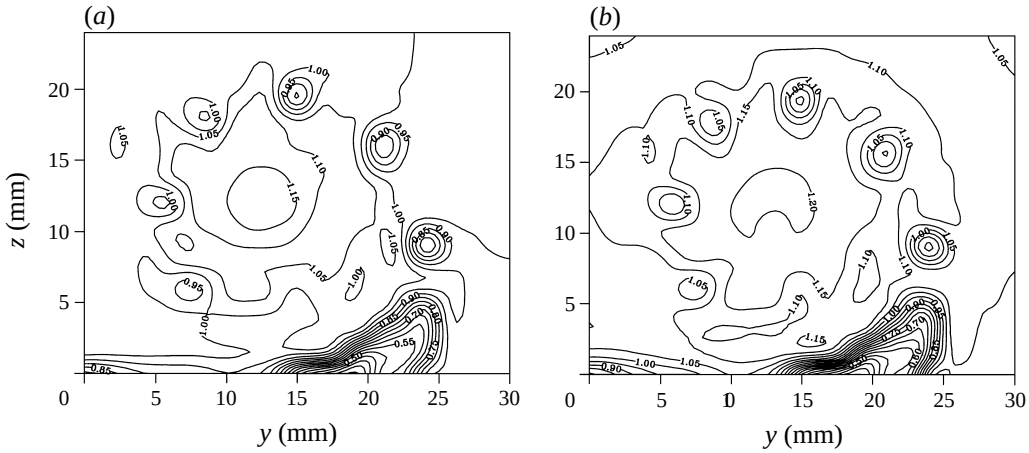

FIGURE 13. Axial velocity (*a*) and total velocity magnitude (*b*) showing the low-momentum regions associated with the streamwise vortical structures. The velocities have been non-dimensionalized with respect to the free-stream velocity: $\alpha = 12.5°$; $x/c = 0.6$; $Re_x = 131\,350$; $U_\infty = 6.79\ \mathrm{m\,s^{-1}}$; $\Delta(y, z) = 0.75$ mm.

local flow, so that the structures can be recognized as pockets of low-momentum flow when they are near the leading edge of the wing. It may be noted that this effect is opposite to that of the main vortex core, where the axial velocity increases towards the core axis, at least prior to vortex breakdown. The wake-like profiles of the sub-vortices disappear as they are wrapped around the main vortex, similar to the diffusion of the axial vorticity component in figure 10 (*c*). The low-momentum aspect of these structures outside the main vortex core was also apparent in the total velocity distribution shown in figure 13 (*b*), and has been observed by previous workers from Pitot traverses (e.g. Payne 1987).

The progression downstream of one of the sub-vortices was mapped by obtaining ten planes of data between $x/c = 0.6$ and $x/c = 0.687$ at a constant chordwise spacing (figure 14). The velocity vector at the centre of the vortex was used to determine the

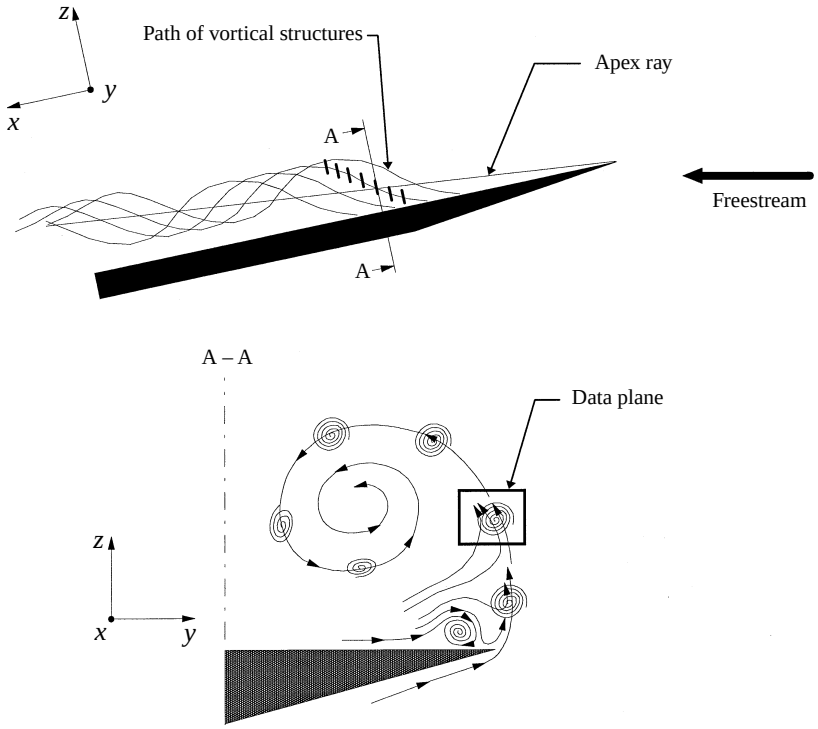

FIGURE 14. Streamwise and cross-sectional schematics of the flow field around the leading edge, illustrating the vortical flow field and the data planes used in acquiring the velocity data in figures 15 and 16.

coordinates of the next downstream plane. Using figure 10 (*d*) as an example, the ten planes of data corresponded to following a sub-vortex from an angular position of about −20° to 80°, using the centre of the main vortex as the origin. The circulation of the vortical structures, calculated around several vorticity contours of magnitude −100/−150/−200, was plotted against the chordwise distance at each downstream station. The result in figure 15 shows that the general trend as the streamwise vortex passes around the main vortex is a gradual decrease in circulation corresponding to the apparent trends in figure 10. However as the contour level, around which the circulation was calculated, was increased the results nearest the leading edge showed an increase in circulation prior to the decrease.

The axial velocity and total velocity magnitude distributions in figure 13 showed that the sub-vortices are represented by a wake-like profile near the leading edge of the wing. As the sub-vortices pass around the main vortex and are wrapped into the core, figure 13 shows that the deficit in velocity with respect to the free-stream flow disappeared. Clarification of the acceleration of the sub-vortical core flow can be seen in figure 16 which plots the change in axial velocity distribution against the radial distance (r) from the centre of the same sub-vortex that was tracked in figure 14.

3.3. *Transition/turbulence*

The start of the transition to turbulence was recorded at $Re_x \approx 1.29 \times 10^5$ and was initially based on the first indication of unsteadiness within the flow field at the

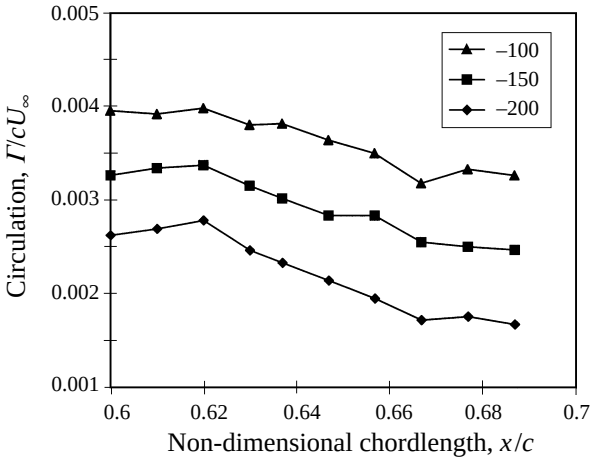

FIGURE 15. Change in the circulation of the vortical structure as it progresses downstream. The circulation has been calculated around vorticity contours of varying magnitude: $\alpha = 12.5°$; $Re_c = 218\,900$.

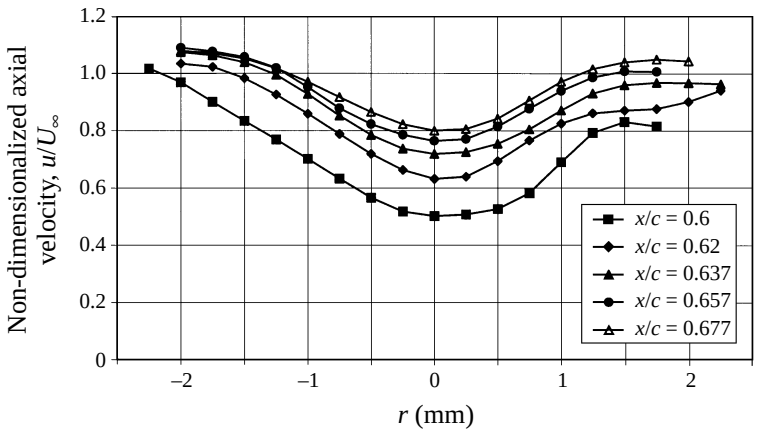

FIGURE 16. Variation in the axial velocity across the core of the sub-vortex as it passes around the main vortex: $\alpha = 12.5°$; $Re_c = 218\,900$.

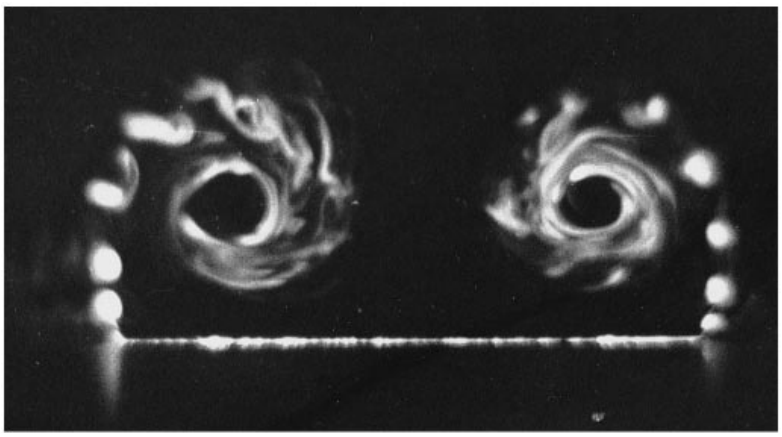

FIGURE 17. Cross-sectional flow visualization of the transitional flow field, where the first signs of unsteadiness appear in the inner spirals: $\alpha = 12.5°$; $x/c = 0.6$; $Re_c = 128\,000$.

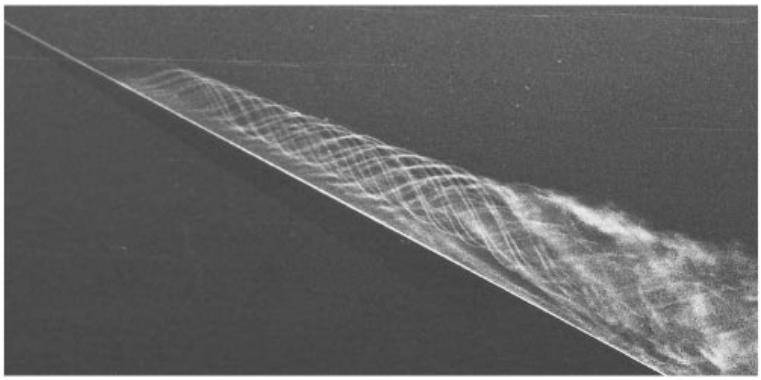

FIGURE 18. Side-on view of the flow field from Lowson (1988) over an 80° delta showing the upward curvature of the vortical structures near the leading edge of the wing and the laminar inner spirals: $\alpha = 30°$; $Re_c = 73\,200$.

leading edge. However, the first appearance of unsteadiness within the flow field was not always at the leading edge. Figure 17 shows a cross-section of the flow field at $Re_x = 1.28 \times 10^5$ where the inner spiral has lost any stable structure. As the local Reynolds number was increased this unsteadiness moved back around the shear layer towards the leading edge. This was contrary to the visualizations of Lowson (1988) who found transition to be caused by an interaction between the K–H and steady instabilities, which appeared initially at the leading edge. Figure 18 shows how transition progresses from the leading edge, around the free shear layer, with laminar structure still present within the inner spirals. Both forms of transition described above have been found in these experiments. The appearance of the K–H instability could well be externally induced, as noted in § 3.1, and transition is known to be a highly sensitive phenomenon. Hence a possible explanation is that this variation in transition mechanisms is a function of the experimental set-up.

Any variation between the two transition mechanisms was found to be within the experimental error for the measurements (2% of the chord length) and hence the data presented in figures 5 and 8 are still valid. The chordwise position of transition and fully turbulent flow, for both sides of the wing, was found to be symmetrical after careful adjustment of the yaw angle.

The concentrated vorticity contained within the sub-vortices is dispersed by the onset of turbulence and under these conditions they cannot be detected from flow visualization, see figure 4 (*d*). Figure 19 shows axial root-mean-square (r.m.s.) velocity distributions for two flow fields, one prior to transition and the other when the vortex is fully turbulent. Over a relatively small change in Reynolds number the axial r.m.s. has increased by almost 400% close to the leading edge of the wing. The distribution of the r.m.s. term has also changed dramatically with peaks of r.m.s. in the pre-transition field corresponding to the positions of the vortical structures. In the turbulent field there is no sign of these r.m.s. peaks and, in fact, the highest r.m.s. values are concentrated in the leading-edge region.

Data taken at higher Reynolds numbers, beyond the transition to turbulence and up to 1×10^6 based on full chord, have revealed that the streamwise vortices remain, although not in the concentrated vortical forms that are easy to detect at lower Reynolds numbers. Figure 20 (*a–d*) shows the axial vorticity distributions at several Reynolds numbers where pockets of vorticity can be seen evenly spaced around the

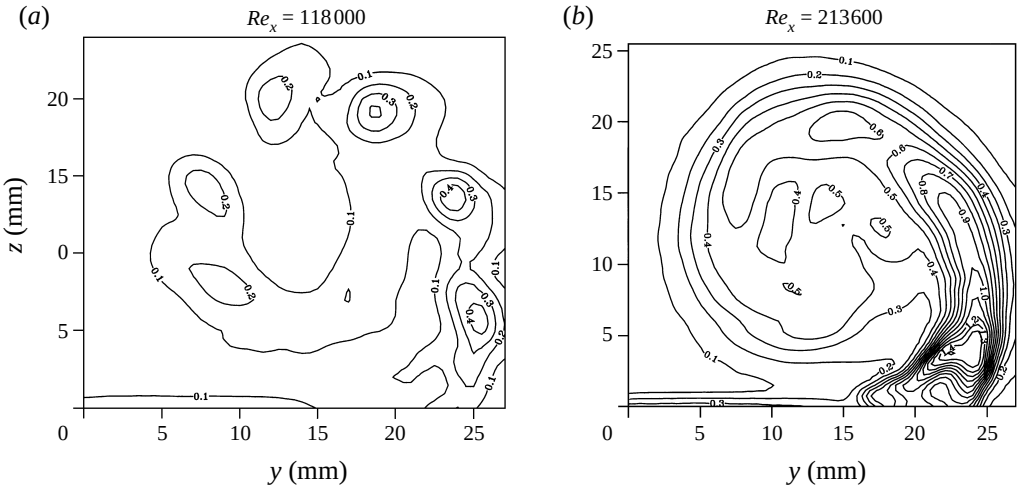

FIGURE 19. Change in the r.m.s. velocity that occurs between the sub-vortical laminar flow field and the fully turbulent flow field: $\alpha = 12.5°$; $x/c = 0.6$; $\Delta(y, z) = 0.5$ mm.

Re_x	λ/x
300 000	0.026
462 200	0.026
599 700	0.028

TABLE 2. Variation in the turbulent wavelength for increasing Reynolds number.

shear layer at a wavelength similar to that seen at pre-transitional Reynolds numbers, as shown in table 2. In these contour plots the structure in the shear layer has been emphasized by decreasing the contour spacing in this region compared to that within the main vortex core.

4. Development of the flow field at the leading edge

Initial studies of the flow showed that there were localized regions of vorticity of opposite sign to that of the main shear layer near the leading edge (Lowson *et al.* 1995). It was therefore unclear if the formation process involved vortices of opposite sign being generated with subsequent diffusion into the shear layer, or if vortices of the same sign as the shear layer were generated from the start. A further question was whether the instability process only started within the free shear layer, or if disturbances in the boundary layer on the pressure surface of the wing were the origin of the process. Detailed measurements near the leading edge have given a clear answer to these questions.

4.1. *The two-dimensional flow field at the leading edge*

Initial studies were undertaken on the pressure side of the wing. Detailed surveys of the boundary layer approaching the leading edge were made. The data showed no evidence of any structure within the laminar boundary layer which could be related to the free shear layer instabilities. Additionally, experiments undertaken over 85° delta wings with much smaller thickness/chord ratios (see table 1) showed no discernible

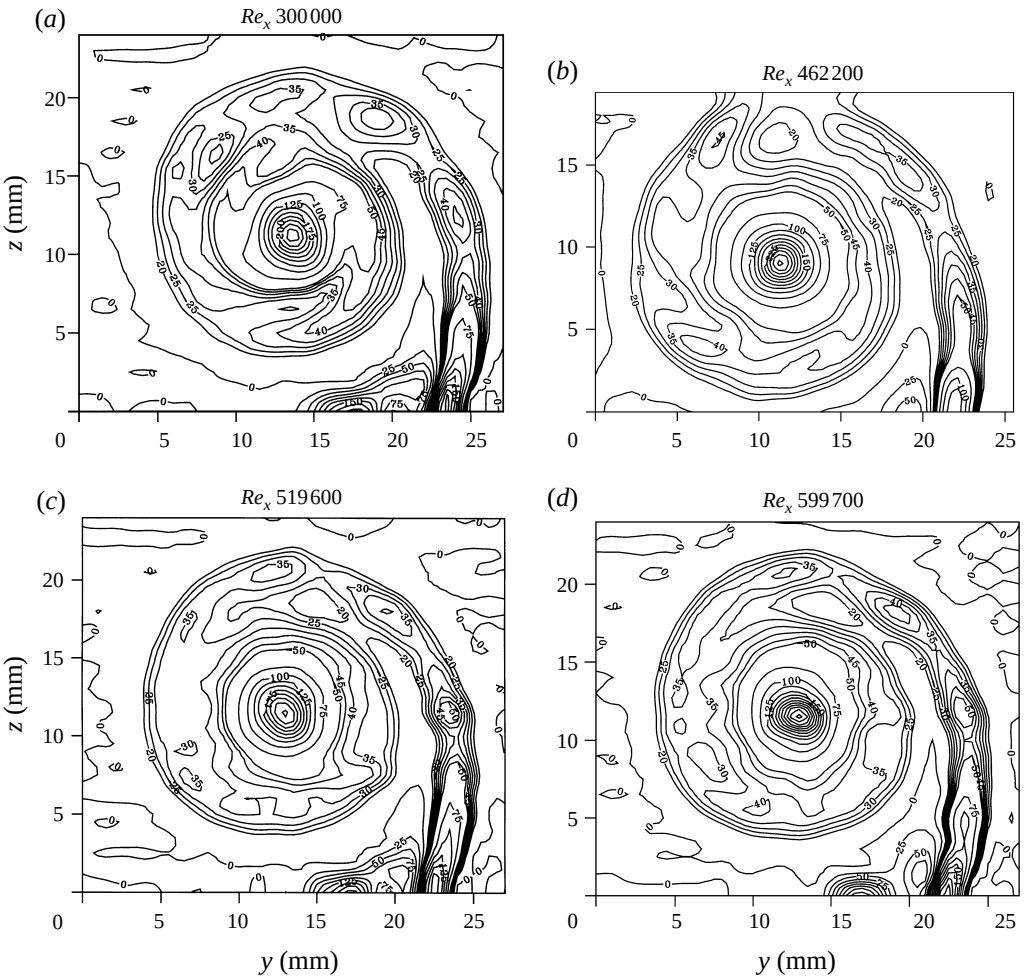

FIGURE 20. Axial vorticity component showing the shear layer structure still remaining, even at Reynolds numbers beyond the transition to turbulence. The contour spacing has been increased within the free shear layer in order to highlight the structure present: $\alpha = 12.5°$; $x/c = 0.6$; $\Delta(y, z) = 0.5$ mm.

difference in the structure of the leeward flow field. The pressure-side boundary layer was therefore discounted as a potential source mechanism.

Thus it was assumed that the streamwise vortices are characteristic instabilities of the free shear layer, and it will be the development of the separated windward boundary layer beyond the leading edge of the wing, in conjunction with fluid from the wing surface, which will determine how and where the streamwise vortices form. An extended grid of data, including a section of the windward flow field, was taken in a plane normal to the wing surface and in the spanwise direction (y, z-plane), as depicted in figure 21. Figure 22 presents a two-dimensional vector plot for the in-plane velocity component of the flow field around the leading edge of the wing. It should be noted that the origin of the coordinate system is arbitrary for this set of data and is not related to the origin of the body-fixed axes. The velocity distribution in figure 22 shows that the outer stream of fluid is faster than the inner stream of fluid for the curved shear layer that leaves the leading edge.

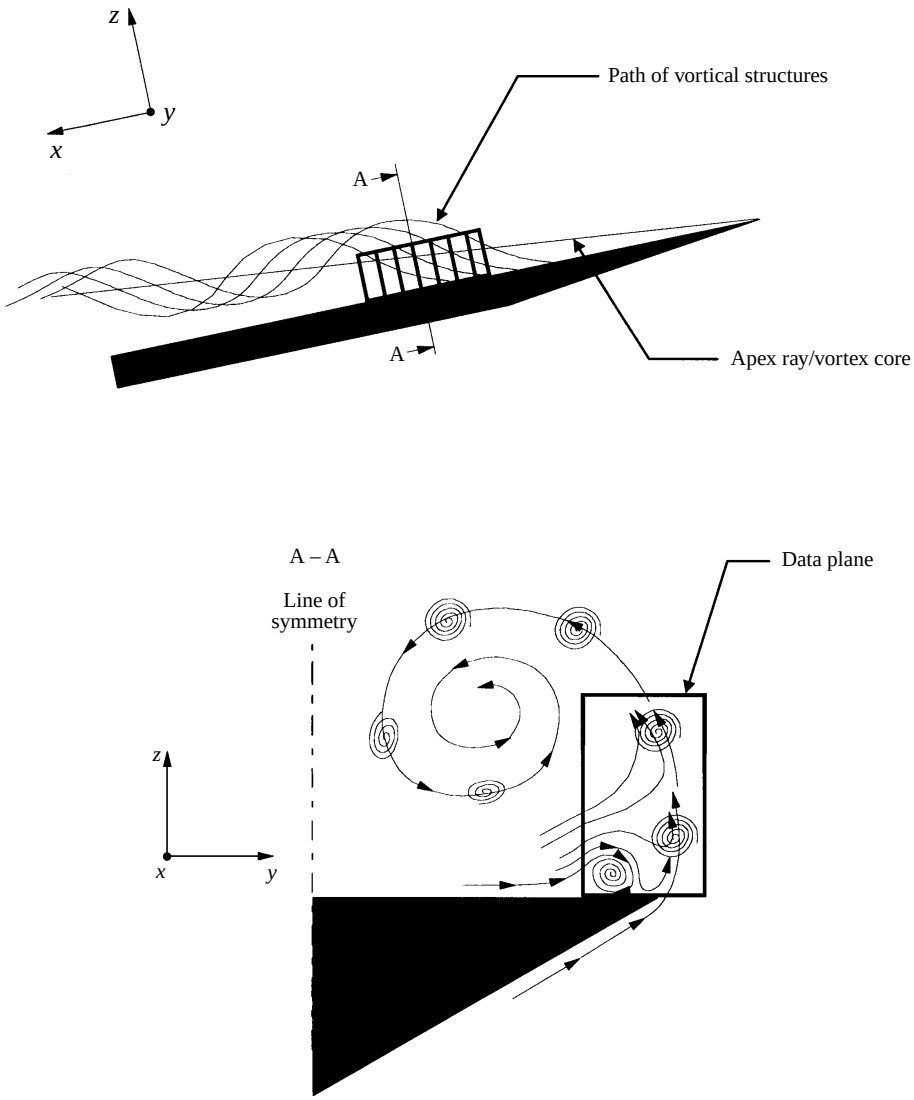

FIGURE 21. Streamwise and cross-sectional schematics of the flow field around the leading edge, illustrating the vortical flow field and the data planes used in acquiring the velocity data in figures 22–27.

Figure 23 shows the two-dimensional streamline distribution for the same case, clearly illustrating the secondary vortex, the reattachment of the secondary vortex inboard of the leading edge and the subsequent flow away from the leading edge. Figure 24 presents the axial vorticity distribution where negative vorticity from the windward boundary layer diffuses rapidly inboard from the leading edge. The vorticity distribution shows the formation of a vortical structure above the leading edge of the wing. The discrepancies near the lower wing surface in figure 24 are due to the square grid structure near an angled surface. The distribution of velocity around the leading edge showed that the position of the wing leading edge correlates well with the high velocity gradients representing the separated windward boundary layer.

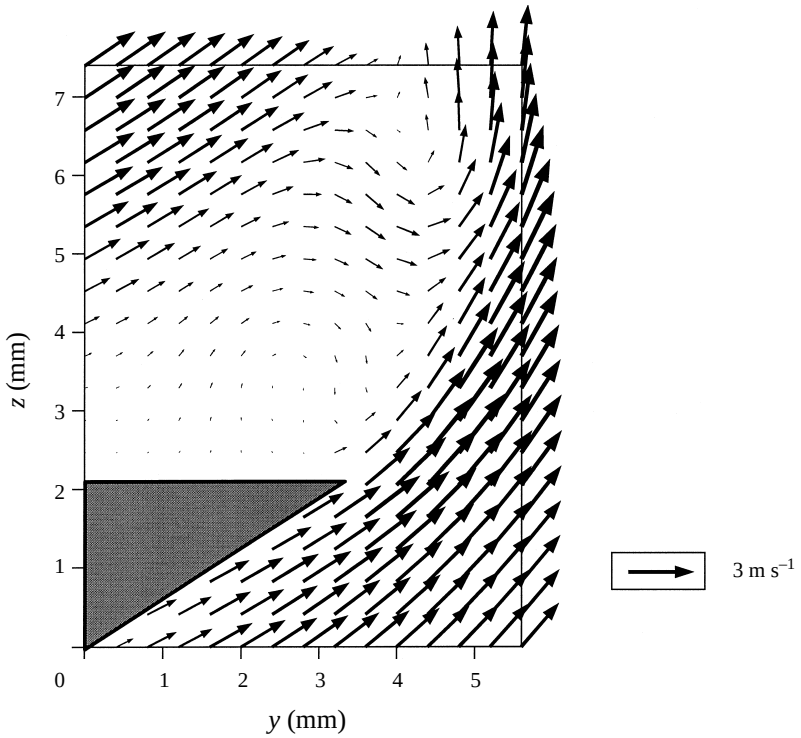

FIGURE 22. Vector map of the flow field around the leading edge of the wing: $\alpha = 12.5°$; $x/c = 0.6$; $Re_x = 121\,900$; $\Delta(y, z) = 0.2$ mm; vector $\Delta(y, z) = 0.4$ mm.

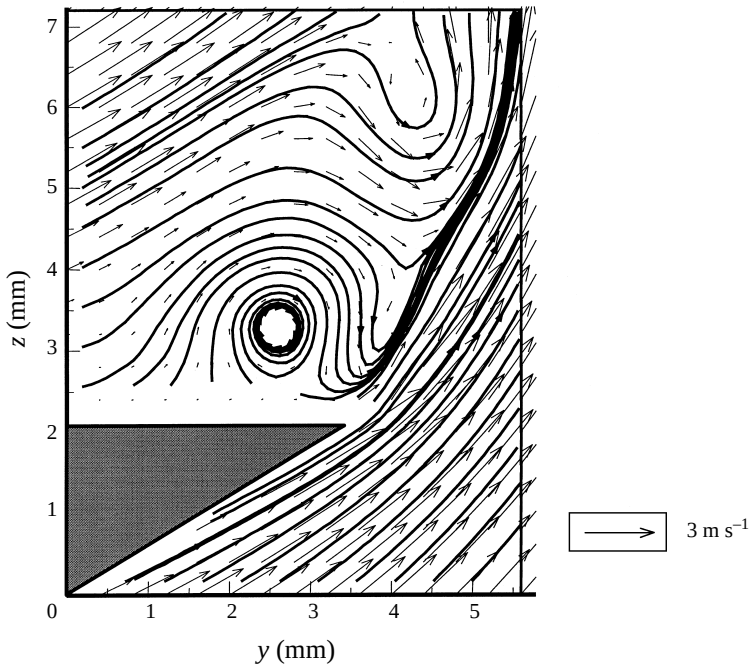

FIGURE 23. Streamline distribution of the flow field around the leading edge of the wing: $\alpha = 12.5°$; $x/c = 0.6$; $Re_x = 121\,900$; $\Delta(y, z) = 0.2$ mm; vector $\Delta(y, z) = 0.4$ mm.

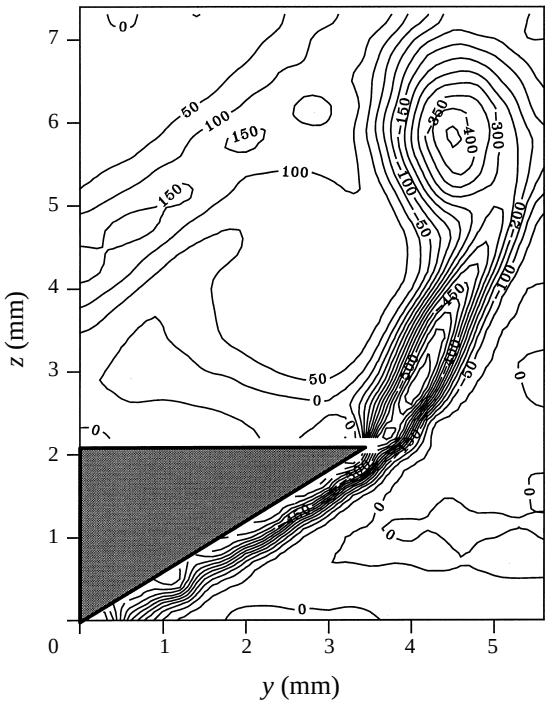

FIGURE 24. Axial vorticity distribution of the flow field around the leading edge of the wing: $\alpha = 12.5°$; $x/c = 0.6$; $Re_x = 121\,900$; $\Delta(y, z) = 0.2$ mm.

4.2. *The downstream development of the leading-edge flow field*

Measurements were taken within a series of planes between $x/c = 0.568$ and 0.600, at a step-size of $x/c = 0.004$ (figure 21), detailing the region of flow between the formation of two streamwise vortices. The three-dimensional data set in figure 25 (see p. 67) shows the development of the axial vorticity at the leading edge. The position of the wing over the spanwise width of the data planes has also been included, although it should be noted that the origin of the data planes is 1 mm above the surface of the wing ($z/c = 0.002$). It can be seen how the shear layer breaks up as each vortex is formed and moves away from the leading edge. Figure 26 shows the two-dimensional plane at $x/c = 0.594$ where fluid of a positive vorticity is clearly being drawn into the shear layer from the secondary vortex region by vortex 1 (labelled on the figure) as it moves away from the leading edge. The process through which this fluid interacts with and is drawn into the leading edge shear layer was found to be extremely consistent. There was no sign of unsteady flow from the LDA data suggesting, together with the previous point, that the process is steady in its nature. Thus the presence of vortices of opposite sign near the leading edge, originally noted by Lowson *et al.* (1995), is found to be due to local entrainment of fluid from the secondary separation region, and not to be part of the instability process itself. Figure 27 shows a two-dimensional vector plot overlaying the axial vorticity distribution of figure 26, the latter being represented by flooded contours in a grey scale, confirming the complex interaction between the secondary vortex and the free shear layer.

The trajectory of a vortical structure over the acquired data planes, based on the centre of its axial vorticity distribution, was at an angle of $14° - 15°$ to the wing surface (x, z-plane), as it progresses downstream alongside the secondary vortex

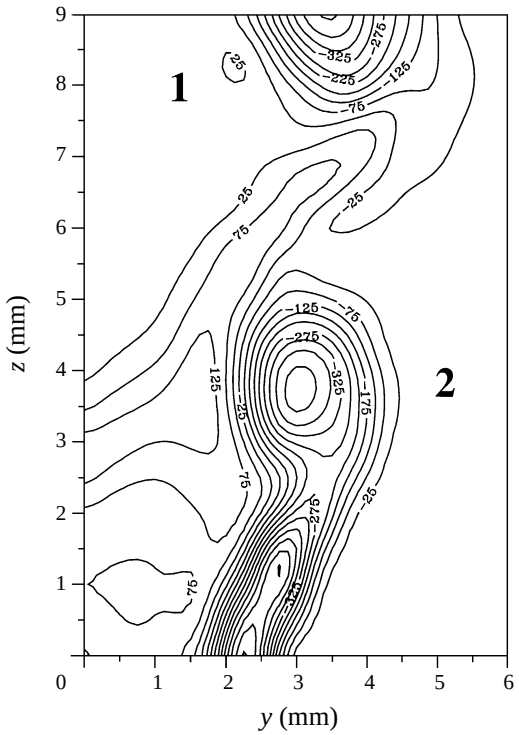

FIGURE 26. Variation in the axial vorticity distribution of a streamwise vortex formed at the leading edge of the wing: $\alpha = 12.5°$; $x/c = 0.594$; $Re_c = 174\,300$; $\Delta(y, z) = 0.25$ mm.

($0.005 > z/c > 0.01$, cf. figure 25). As the sub-vortex moves away from the leading-edge region the trajectory moves into line with the outer inviscid flow (approximately 30° above the wing surface) as the influence of the secondary vortex becomes less (see figure 18).

4.3. *Free shear layer velocity profiles*

Detailed velocity profiles taken through the interface of the free shear layer were obtained in a spanwise direction (y, z-plane), at various heights above the wing surface, for $x/c = 0.6$. Figure 28 (*a–c*) shows the three components of velocity, non-dimensionalized with respect to the free-stream velocity, at a local Reynolds number where vortical structures are forming near the leading edge.

- The axial velocity (u/U_∞) shows the profile of the separated windward boundary layer which contains the classic inflection point due to diffusion of velocity between the two streams of fluid and normally associated with the K–H instability in plane mixing layers. As the height increases, away from the wing surface, the free shear layer moves outboard from the leading edge, as can be seen also from the previous vector and velocity plots (figures 22 and 23).
- The spanwise velocity (v/U_∞) is initially large in the outboard direction as the windward flow negotiates the leading edge of the wing. Also near the surface, inboard of the leading edge, there can be found a change of direction in the spanwise velocity representing the reattachment point of the secondary vortex. As the flow moves away from the surface the spanwise velocity tends to zero corresponding to the rotation of the velocity vectors past the leading edge (figure 22).

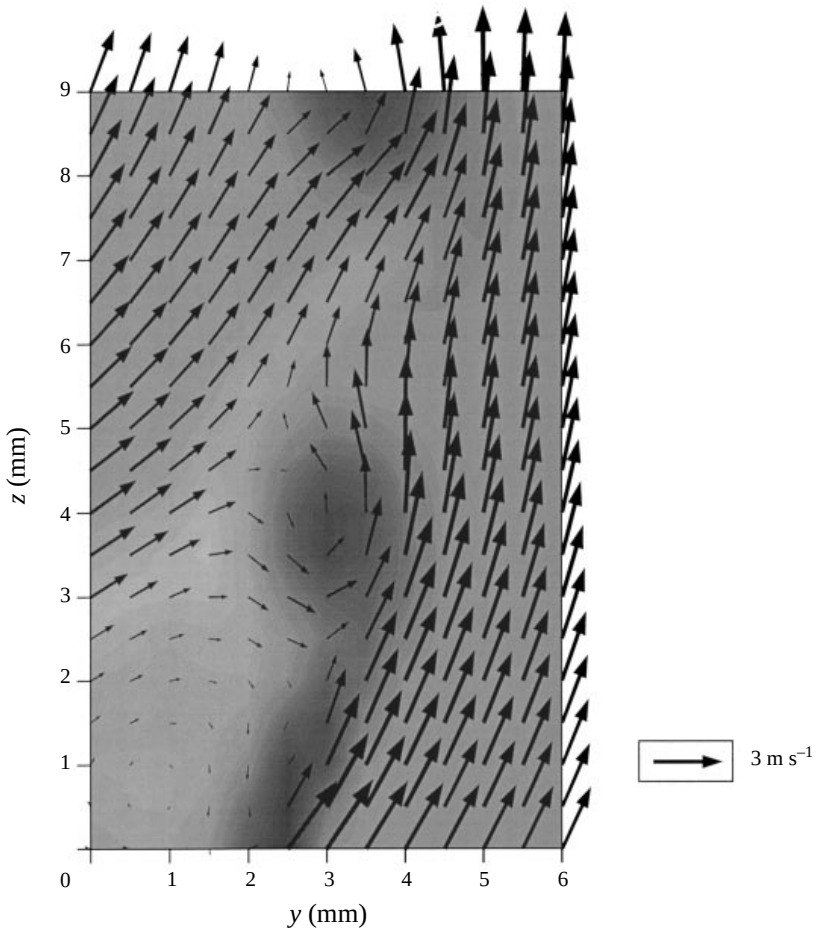

FIGURE 27. Overlay of vectors on the axial vorticity distribution, illustrating the combination of fluid from both the upper and lower surfaces in the formation of the vortical structure: $\alpha = 12.5°$; $x/c = 0.594$; $Re_c = 174\,300$; $\Delta(y, z) = 0.25$ mm; vector $\Delta(y, z) = 0.5$ mm.

• The vertical component of velocity (w/U_∞) incorporates a large inflection point that does not correspond to the position of the inflection point in the axial velocity. As the distance increases from the surface of the wing it can be seen that the inflection point in the vertical velocity remains at the same relative position in the free shear layer, corresponding approximately to the minimum in the axial velocity.

The total velocity distribution in figure 29, for $z = 1.1$ mm off the surface ($z/c = 0.002$), indicates that the interface of the free shear layer is located at $y \approx 2.7$ mm based on the local minimum in velocity. The point of inflection in the vertical velocity was found to correspond to this local minimum and can also be related to the position of maximum axial vorticity in the free shear layer. By $z = 4.1$ mm ($z/c = 0.009$) the point of inflection in the vertical velocity corresponds to the centre of a sub-vortex. If the flow field is assumed to be conical, then the sub-vortices can be said to form at the interface of the free shear layer. This is also apparent from the vorticity distributions in figure 25.

If the velocities at $z = 1.1$ mm are resolved into the direction of the interface vector then it can be seen that the inflection point in the resolved vertical component

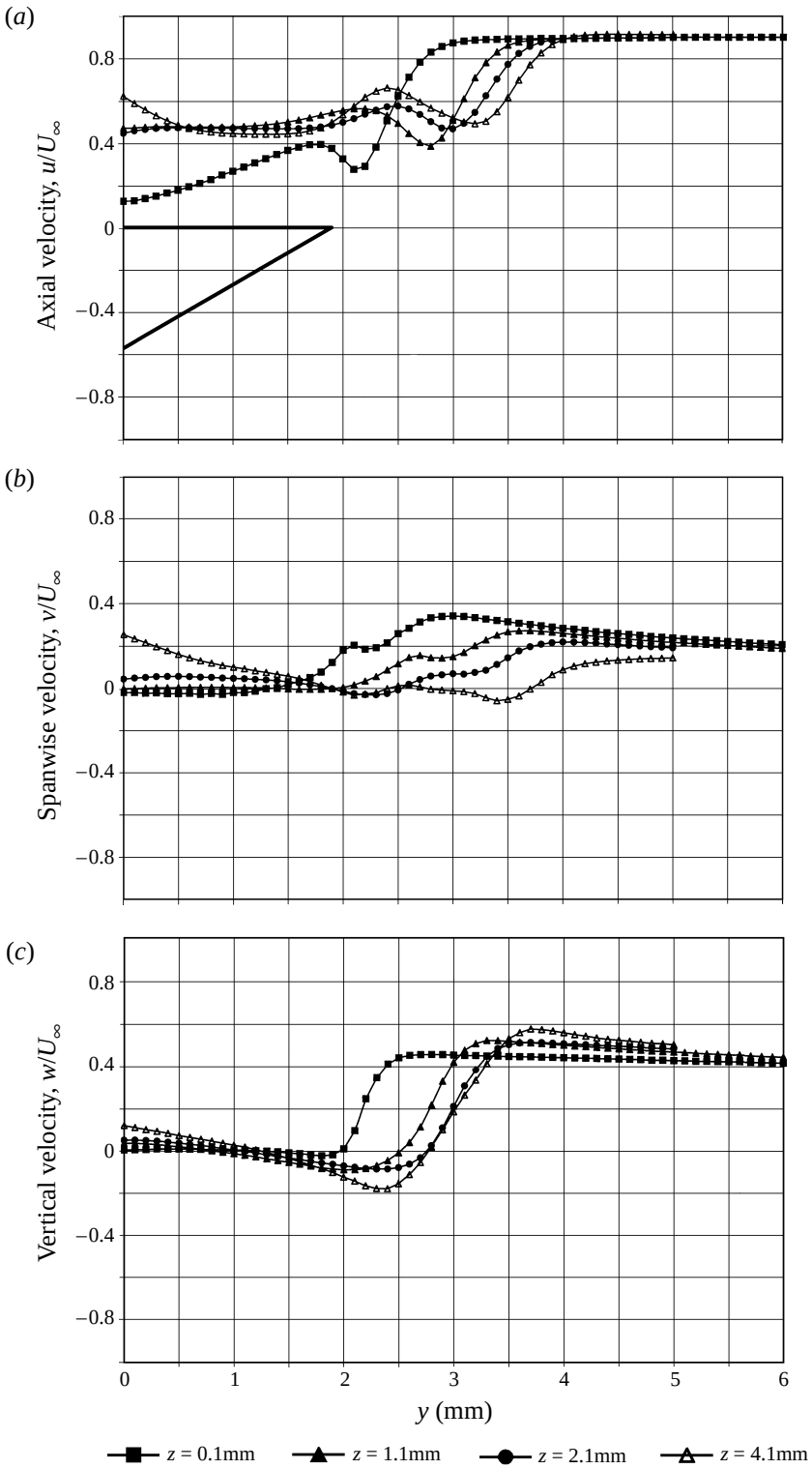

FIGURE 28. Variations in the three components of velocity at the leading edge of the wing, with increasing distance off the wing surface (non-dimensionalized with respect to the free-stream velocity): $\alpha = 12.5°$; $x/c = 0.6$; $Re_x = 11\,800$; $\Delta(y, z) = 0.1$ mm.

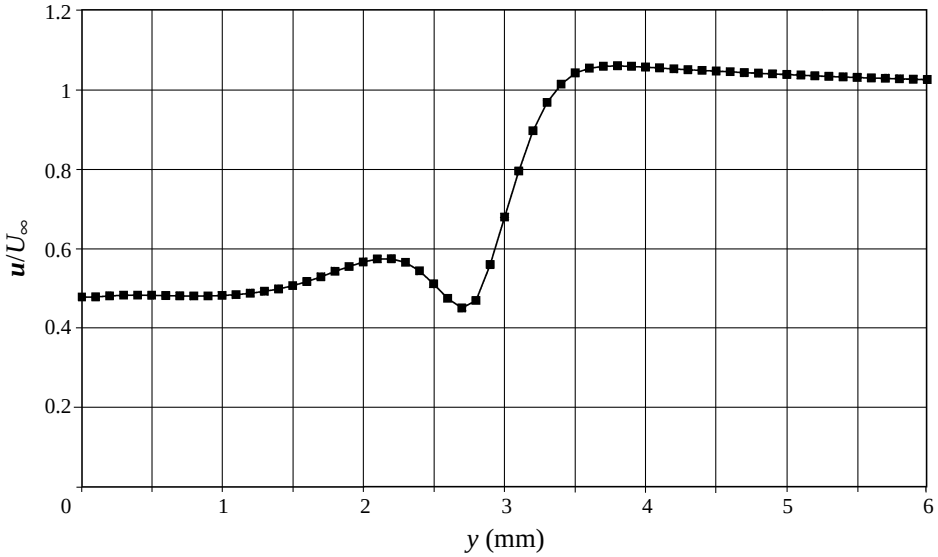

FIGURE 29. Variation in the total velocity magnitude at the leading edge of the wing: $z = 1.1$ mm; $\alpha = 12.5°$; $x/c = 0.6$; $Re_x = 118\,000$; $\Delta(y, z) = 0.1$ mm.

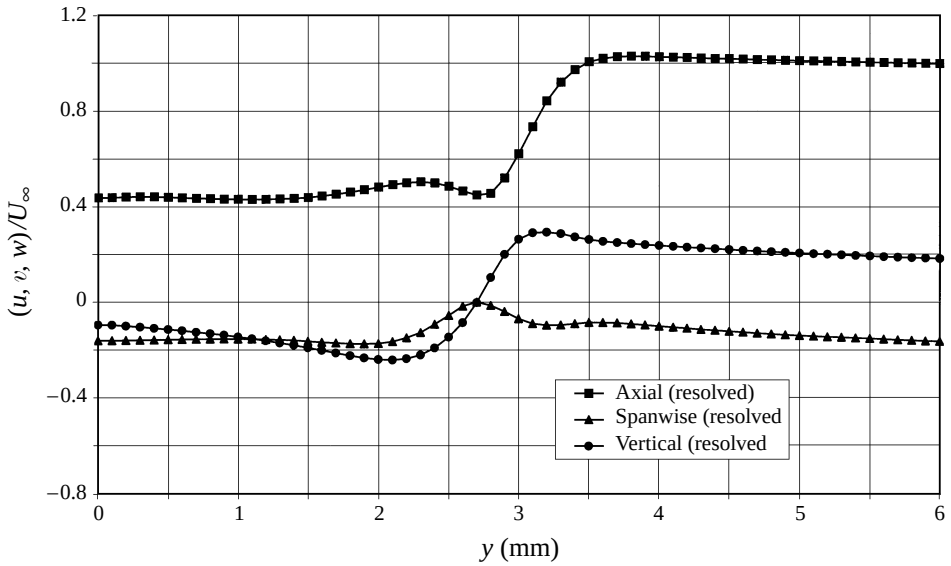

FIGURE 30. Variation in the velocity components, resolved in the interface vector direction, at the leading edge of the wing: $z = 1.1$ mm; $\alpha = 12.5°$; $x/c = 0.6$; $Re_x = 118\,000$; $\Delta(y, z) = 0.1$ mm.

remains at the interface of the shear layer (figure 30). However, the surrounding data points are no longer coincident with the resolved set of axes. The axis transformation was 18.4° in the longitudinal plane (x, z) and 35.0° in the lateral plane (x, y), which means that the local data points around the interface are less than 0.3 mm off the resolved axes. Hence, due to the axial derivatives being small, the point of inflection will almost certainly still be at the interface. This was confirmed by interpolating

the volumetric data set presented in § 4.2 (cf. figure 25) and extracting the relevant velocity profiles.

The trajectory of the interface (and hence the position of inflection) decreases from 18° to 14°, relative to the wing surface in the (x, z)-plane, over the range $0 < z/c < 0.004$. This range of z/c is prior to the formation of any sub-vortices. The trajectory correlates well with the trajectory of the vortical structure, obtained over the range $0.005 < z/c < 0.01$, cf. figure 25. A two-dimensional inflection point, stationary with respect to the main flow, is known to produce co-rotating vortices in a simplified two-dimensional boundary layer as shown by Stuart (Gregory *et al.* 1955). However, in this case the flow field surrounding the free shear layer inflection point has a significant spanwise component and the trajectory of the inflection point in the (x, y)-plane continually changes as the free shear layer leaves the leading edge, cf. figure 22.

Data were also obtained at the same position over the wing at the local Reynolds number in figure 4 (*a*) where the free shear layer does not exhibit vortical structures. It could be seen that there is still an inflection point in the vertical component of velocity that corresponds to the interface of the free shear layer. However, in this case vorticity is quickly diffused as the free shear layer moves away from the wing surface and it does not congregate into vortices.

5. Discussion of the steady instability

5.1. *Source of the instability*

The streamwise vortical structures that develop with increasing Reynolds number follow a helical path into the core of the primary vortex and are highly three-dimensional in nature. The strength of the sub-vortices decreases as they progress around the main vortex, due to the diffusion of vorticity. However, a small region of growth was found near the leading edge where the sub-vortices are formed. Three-dimensional instability structures are known to appear in both two-dimensional and three-dimensional shear flows. In three-dimensional shear flows streamwise instabilities can occur as the primary instability, as a direct consequence of the curvature of the flow (Gregory *et al.* 1955; Poll 1985).

5.1.1. *Curvature effects*

Two sources of curvature have been identified in the leading-edge region over the 85° delta. The first source was due to the flow having to negotiate the sharp leading edge and can be associated with centrifugal effects. The consequence of the centrifugal instability concept (Rayleigh 1916) for curved free shear layers has recently been examined by Liou (1994). Centrifugal effects have a destabilizing effect if the inner stream is faster. In the case of the delta wing the presence of the secondary vortex stabilizes the shear layer with respect to centrifugal instability near the leading edge, cf. figure 22. In physical terms, the shear layer is stable to any overturning/centrifugal instability that would try to throw fluid out from the inner stream. In mathematical terms, the square of the circulation does not decrease in the radial direction.

Liou analysed the instability of a curved shear layer with a higher speed inner stream. He found that the characteristic form of instability in the free shear layer was as pairs of contra-rotating vortices, similar to the Taylor–Görtler instability observed in a boundary layer. This is obviously different from the co-rotating vortex instability found in the present case. On the other hand, away from the leading edge and associated secondary separation, at higher Reynolds numbers when the rolled-up

shear layer is more fully formed, there will be an increase in velocity passing inwards through the shear layer towards the concentrated vortex core. Thus there would be the prospect of a centrifugal instability under these conditions, and it is possible that this effect plays a role in transition of the free shear layer at higher Reynolds numbers.

There is also a second source of curvature in the downstream plane where streamlines are turned vertically relative to the wing surface (figure 18). However, this source of curvature occurs after the formation of the sub-vortices has begun and well past the leading edge. Hence it appears that this second curvature is also unlikely to be responsible for the formation of the sub-vortical structures.

5.1.2. *Vortex sheet instabilities*

The distribution of the axial vorticity at the leading edge of the wing (figure 24) showed that, although negative vorticity is initially produced within the windward boundary layer, it diffuses rapidly across and inboard of the leading edge. In conjunction with the velocity distributions the position of the maximum axial vorticity was found to correlate with the interface of the free shear layer, as would be expected. This three-dimensional vortex sheet, that springs from the leading edge of the wing, then rolls up to form the primary vortex. As discussed in the Introduction, the instability of vortex sheets is generally dominated by K–H-type instabilities. The unsteady vortical structures in the free shear layer of a delta wing, found by several investigators, have been essentially two-dimensional, and sprung from the whole of the leading edge. They have a strong resemblance to the spanwise vortical structures found in a two-dimensional mixing layer (Winant & Browand 1974) and hence have been associated with the K–H instability. It should be noted that in the present case the steady instabilities observed are localized. If the association of the unsteady quasi-two-dimensional structures with the K–H instability is correct, then the principle of the K–H instability, which is based on two-dimensional arguments, can also be applied to a highly three-dimensional vortex sheet. Taking this a step further, if the latter is the case, then disturbances can be amplified by the K–H instability mechanism in any plane perpendicular to the vortex sheet. This is an important concept regarding the amplification of disturbances in a three-dimensional vortex sheet.

The K–H instability mechanism itself has been covered previously, a good example being Batchelor (1967, pp. 511–517). Other relevant theories, also connected with the instability of a vortex sheet, have been put forward. Rayleigh's inflection point theorem for an inviscid fluid, based on a linear analysis of an inflectional velocity profile (resembling a simple mixing layer), showed that disturbances would amplify at the position of inflection (Rayleigh 1880). The vanishing of the vorticity gradient is a criterion for instability put forward by Lin (1945) in a physical interpretation of Rayleigh's inflection point theorem. An inflection point in a two-dimensional flow represents the position where the vorticity gradient is zero. Based on the analysis of the flow field in terms of vortex lines, disturbances can be amplified at the inflection point due to the restoring tendency of the surrounding vortex lines being impaired. However, all these theories are based on simplified flows, whereas the free shear layer in this case is highly three-dimensional.

Analysis of the leading-edge region in § 4 found that the vortical structures form at the interface of the free shear layer. The detailed free shear layer velocity profiles in figure 28 showed that there are major inflection points in both the axial and vertical components. However, only the inflection point in the vertical component is present at the interface and can be related to the maximum axial vorticity. If the vertical

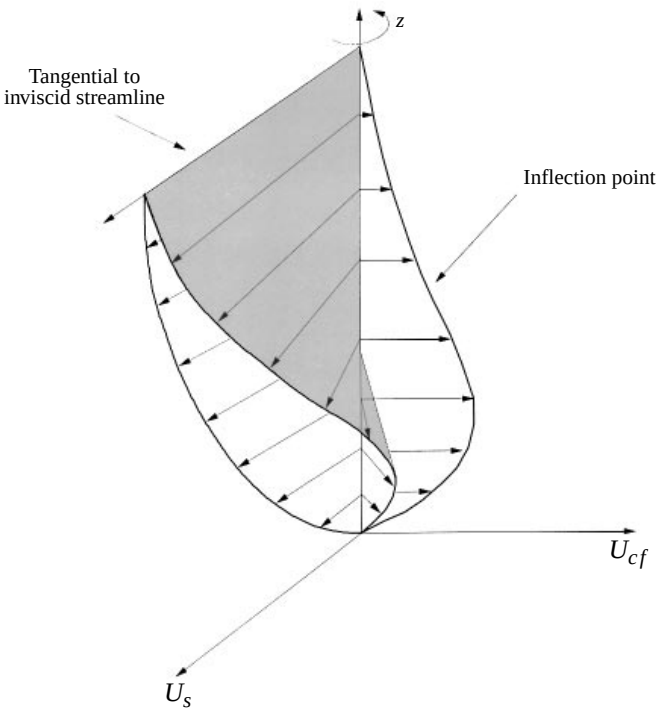

FIGURE 31. The velocity distribution over a swept wing showing the inflection point in the cross-flow velocity profile.

velocity profile could be analysed purely as a two-dimensional flow field, it would be remarkably similar to the classical profile across two parallel streams of fluid and hence subject to the K–H instability mechanism. Mathematically the velocity profile is also dynamically unstable (Fjortoft 1950); however this is still not a sufficient criterion for instability by itself (Drazin & Reid 1981). Figure 30 showed that when the components of velocity are resolved with respect to the interface vector, the inflection point in the resolved vertical plane (or more correctly the 'critical' cross-flow plane, see § 5.1.3) remains at the free shear layer interface, and is now stationary with respect to the interface vector. If the K–H instability mechanism could amplify disturbances in this plane, which is perpendicular to the interface vector and hence the vortex sheet, the result would be a system of stationary, co-rotating vortices

5.1.3. *The case for the cross-flow instability*

Parallels can also be drawn here between this three-dimensional free shear layer instability and the simpler case of the cross-flow instability found in boundary layers over swept wings/cylinders and rotating disks. This is an inertial instability, also occurring as a series of fixed-wavelength, co-rotating vortices and is accepted to be due to an unstable inflection point in the cross-flow velocity profile (Saric & Reed 1988). For the case of a boundary layer the cross-flow velocity profile (U_{cf}) is usually defined as being perpendicular to the inviscid streamline (U_s), as shown in figure 31. A necessary criterion for the production of stationary streamwise vortices in a boundary layer is that this inflection point has zero velocity in the direction of propagation of a disturbance. The comparison between these two instabilities has already been drawn by Washburn & Visser (1994). They noted that the shear layer encounters a pressure

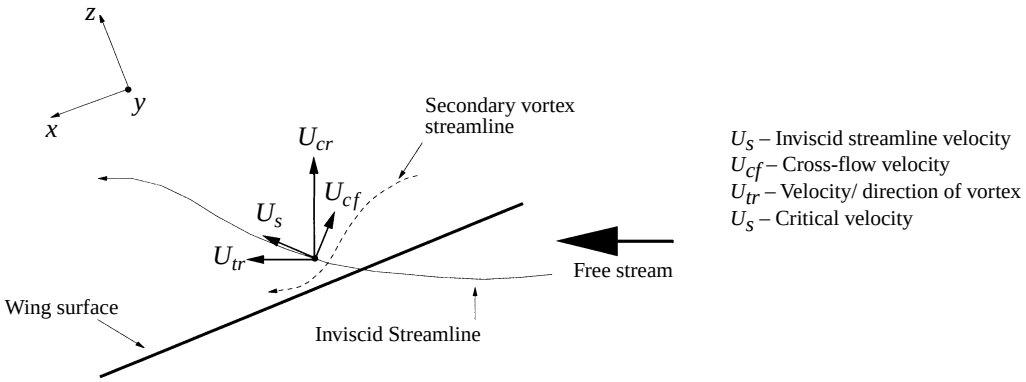

FIGURE 32. Schematic showing the critical velocity profile with respect to the inviscid flow, the secondary vortex and trajectory of the sub-vortices.

gradient as it leaves the leading edge and hence the mean streamlines, aligned with the shear layer, cross this pressure gradient. After the sub-vortices have formed and begun to wind around the main vortex, they followed constant-pressure contours. It is well-known that the pressure gradient is a key factor in the formation of an unstable inflection point, and hence cross-flow-induced vortices, in a boundary layer.

An inflection point is always present in a free shear layer in the main flow direction due to diffusion of velocity across the interface of the free shear layer. In a simple one-dimensional mixing layer there can be inflection points in two directions if the velocity components are resolved in a direction other than the main flow. However, the presence of an inflection point in a plane perpendicular to the main flow direction is due to the highly three-dimensional nature of the two layers of fluid that meet at the leading edge of the delta wing. The key issue here is the presence of the secondary vortex which induces the inner surface velocity vector of the free shear layer to vary from the outer velocity vector. The majority of the pressure field over a delta wing is prescribed by the two main vortices. The presence of these main vortices induces an adverse pressure gradient on the wing surface, which creates separation and the formation of the secondary vortex. This secondary vortex modifies the local pressure field near the leading edge and plays a large part in determining the inner surface velocity vector of the free shear layer. The flow field at the leading edge of the wing is depicted in figure 32. The outer inviscid flow at the leading edge is moving in a direction away from the wing surface. Across the separated shear layer, in a spanwise direction, the velocity vector is rotated into a direction either parallel to or towards the wing surface, depending on the height above the wing surface. This can be deduced from the velocity profiles in figure 28. In essence the experimental data provided here confirm the conclusion of Washburn & Visser that the shear layer crosses a pressure gradient as it leaves the leading edge. This spanwise pressure gradient is due to the presence of the secondary vortex.

The fact that the free shear layer crosses this pressure gradient results in the formation of a stationary inflection point in the plane perpendicular to the direction of the flow in the vortex sheet (figure 30). In cross-flow instability in boundary layers it has been found that the normal to the trajectory of the vortical structures (U_{tr}) is closely associated with the 'critical' profile (U_{cr}), which is defined as the velocity profile where the inflection point has zero velocity (Poll 1985). In the present experiments, it has been found that the trajectory of the stationary point of inflection correlates

with the trajectory of the vortical structures. Hence the critical profile is again closely associated with the normal to the trajectory of the sub-vortices, as shown in figure 33. In other words, this unstable cross-flow inflection point mirrors the case of cross-flow instability in boundary layers.

However, the description of this free shear layer cross-flow instability is, in essence, identical to the concept of a three-dimensional K–H instability mechanism, proposed in § 5.1.2. What differences are there in the concepts of K–H instability and cross-flow instability? If one analyses the velocity profile in figure 31 in terms of the streamwise vorticity vector, it is clear that the vorticity distribution peaks at the position of inflection. A peak in vorticity in the flow field is also representative of a vortex sheet and it may be possible for the same concepts of instability to be applied to both cases. Hence, the formation of these steady, co-rotating sub-vortices is most readily explained in terms of a local three-dimensional K–H-type mechanism.

5.2. *Modelling the delta wing free shear layer*

Recent linear stability analyses of the cross-flow instability over swept wings have taken advantage of improvements in numerical methods to solve the three-dimensional linear stability equations, including the curvature terms (Collier & Malik 1988). However, these solutions still incorporate the parallel flow assumption in order to make the instability analysis a two-dimensional problem. The application of the linearized equations to a curved surface such as the leading edge of a swept wing has many similarities to the development of the free shear layer over a delta wing. Application of the three-dimensional linearized equations to this problem, with the appropriate boundary conditions for a free shear layer, may provide some indication of the instability structure found experimentally. Of course, the local flow around the free shear layer of a delta wing is inherently three-dimensional. Hence for two-dimensional instability concepts to be employed, such as the parallel flow assumption, the spanwise component of flow would have to be ignored. It is not clear without taking a mathematical approach to the problem how significant the effect of this simplification would be. Liou (1994) has already shown numerically that three-dimensional structures, resembling Taylor–Görtler vortices found in boundary layers, form in a curved free shear layer. However, in trying to simplify the flow field in order to analyse it in mathematical linear two-dimensional terms it is easy to lose sight of the more general aspects of three-dimensional instability, such as flow with stretching and interaction of vortex lines (Drazin & Reid 1981).

The deficiencies of Eulerian numerical schemes in modelling a complex, separating flow field, such as a delta-wing free shear layer, have already been pointed out in the Introduction. The application of a Lagrangian-type scheme, which has already been demonstrated successfully by Koumoutsakos & Shiels (1996) on a flat-plate flow field, is an attractive option that may well provide more insights into the development of this complex free shear layer.

In the analogy with the boundary layer cross-flow instability it should be recognized that the stationary inflection point concept is primarily based on mathematical features. As pointed out by Gregory *et al.* (1955), 'a fundamental problem that has not been solved is the reason why a disturbance which appears to be stationary, also appears to be the dominant one over a considerable area of instability'. This is a point that is also applicable to the delta-wing free shear layer and does not appear to have been resolved by more recent work.

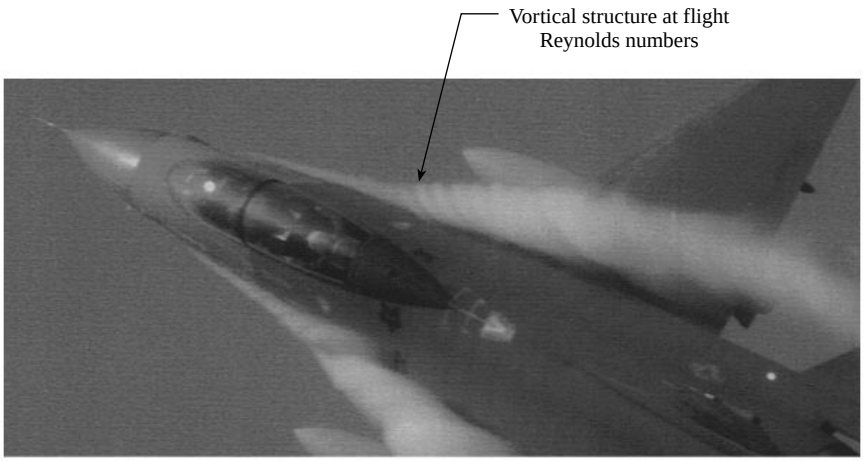

FIGURE 33. Flow field over an F-16 aircraft showing the vortical structures over the LEX made visible by condensation effects.

5.3. *Transitional/turbulent flow*

Results over the 85° delta found the initial transition to turbulence to be dependent on a specific local Reynolds number, confirming the results of Lowson (1988) over an 80° delta wing.

The transition to turbulence dissipates the concentrated vortical structures that characterized the pre-turbulent flow field. However, previous results from investigations by Verhaagen *et al.* (1993) and Visser & Washburn (1994) have indicated that these structures continue to form at Reynolds numbers beyond transition. Also flow visualization obtained over aircraft in flight, utilizing condensation effects in the air (Campbell *et al.* 1989), have shown sub-vortical structures in LEX flow fields. The example shown in figure 33 is an F-16, courtesy of the USAF. These structures have been reproduced at low Reynolds numbers using a 1/32 scale model of the F-16 in this Department's low-turbulence wind tunnel. Based on the instability mechanism put forward in § 5.1.2 for the formation of these structures, which is an inertial instability, it would be reasonable to expect the process to continue at Reynolds numbers beyond transition. Velocity data obtained throughout turbulent vortices has confirmed this hypothesis for the 85° delta in this study (figure 20). The wavelength of the structures was found to be similar at high Reynolds number to that at laminar Reynolds numbers near transition. Also the trajectory of these turbulent vortices correlated with laminar trajectories, the turbulent trajectories being at a slightly greater angle to the wing surface due to the increasing strength of the main vortex.

As with the previous time-averaged velocity data of other investigators the vortical structures are very weak and only become traceable through vorticity data some distance above the leading edge. This is unlikely to be due to the formation process being delayed, although more detailed data in the leading-edge region for a turbulent flow field would be required to confirm this. A more probable explanation was found in the r.m.s. distributions for the turbulent vortex where the highest r.m.s. values were found near the leading edge (figure 19). This could well mask the weak structure to be found in this region.

The technique of LDA, with its time-averaged data, does not lend itself to the quantitative mapping of turbulent flow structures, even steady ones. It is difficult

to form any kind of estimation as to the real strength of the structures. Note that the visualization of the sub-vortices at full scale from condensation is fundamentally different from low Reynolds number smoke visualization. The appearance of the condensation corresponds to low-pressure regions within the vortices. Thus the fact that the sub-vortices become visible at flight Reynolds numbers through condensation effects suggests that the low-pressure region of the sub-vortices is differentiable from the surrounding flow field. A possible solution is the use of a particle image velocimeter (PIV) to obtain an instantaneous picture of the flow field.

The continued formation of these streamwise vortices at high Reynolds number could have possible consequences for modern fighter aircraft. Configurations with large LEX, such as the F/A-18, could suffer fluid/structural interaction as these vortical structures pass downstream. Certainly the F/A-18 has suffered fatigue problems on the two fins downstream of the LEX. The likely reason for this is some kind of periodic forcing of the structure resulting from periodicity in the aerodynamic flow field. Vortex breakdown is the prime candidate for the cause of this interaction. However, it has been found that variations in sweep and angle of attack alter the wavelength of the sub-vortices. Hence the variation in surface pressures on the fins, caused by the downstream progression of these streamwise structures during manoeuvres, could also result in a forcing interaction. Interestingly, the excessive forcing on the vertical fins of the F/A-18 has been alleviated by applying an inboard fence near to the junction of the LEX/main wing. Recent flow visualization studies by Thompson (1997) have shown that the fence induces the formation of a vortical structure at the leading edge of the LEX, that is remarkably similar to the sub-vortices found in present investigations within this Department over 70° delta wings. Interaction between the vortex breakdown and the induced vortex appears to reduce the forcing on the fins. Further research is certainly required to determine whether these kinds of instability structures have either a beneficial, or a detrimental, part to play in this kind of fluid/structural interaction.

6. Conclusions

Simultaneous three-dimensional velocity data have been obtained over an 85° delta wing, at 12.5° angle of attack, for Reynolds numbers ranging from 4×10^4 to 6×10^5. This work, in combination with a comprehensive program of flow visualization experiments, was aimed at providing improved understanding of the steady instabilities previously observed in the curved shear layer. The study has both revealed new aspects of the vortical flow field and confirmed previous conclusions based on flow visualization results.

- The streamwise streaks observed in these experiments and by a number of other investigators, in the free shear layer over delta wings, have been shown to represent a series of fixed-wavelength, co-rotating vortices–all rotating in the same sense as the main vortex core.
- The sub-vortical structures form just downstream of the leading edge of the wing and are a characteristic instability of the free shear layer.
- The flow is found, from both flow visualization results and velocity data, to be a function of local Reynolds number based on distance to the apex
- Based on flow visualization results, the free shear layer undergoes transition to turbulence at a location which is also a function of local Reynolds number. In addition, the length of the transition region appears to be approximately constant.

• The cause of the steady sub-vortices is suggested to be a local three-dimensional Kelvin–Helmholtz instability of the free shear layer, that has parallels to the cross-flow instability observed in three-dimensional boundary layers.

• Detailed velocity data in the leading-edge region have confirmed the existence of a three-dimensional stationary inflection point within the free shear layer, consistent with the formation of steady sub-vortices.

• Velocity data at high Reynolds number have shown that the sub-vortices continue to form at the leading edge of the delta wing. This provides an explanation for the flow visualizations at flight Reynolds numbers over LEXs of fighter aircraft such as the USAF F/A-18 and F-16.

The authors gratefully acknowledge the support of EPSRC in funding this research effort. In addition, we would like to thank the referees for their helpful comments and interpretations.

REFERENCES

Batchelor, G. K. 1967 *An Introduction to Fluid Dynamics*. Cambridge University Press.

Campbell, J. F., Chambers, J. R. & Rumsey, C. L. 1989 Observation of airplane flow fields by natural condensation effects. *J. Aircraft* **26**, 593–604.

Collier, F. S. & Malik, M. R. 1988 Curvature effects on the stability of three-dimensional laminar boundary layers. *AGARD CP* 438, Paper 10.

Doligalski, T. L., Smith, C. R. & Walker, J. D. A. 1994 Vortex interactions with walls. *Ann. Rev. Fluid Mech.* **26**, 573–616.

Drain, L. E. 1980 *The Laser Doppler Technique*. J. Wiley & Sons.

Drazin, P. G. & Reid, W. H. 1981 *Hydrodynamic Stability*. Cambridge University Press.

Fjortoft, R. 1950 Application of integral theorems in deriving criteria for stability for laminar flows and for the baroclinic circular vortex. *Geofys. Publ., Oslo* **17**, 1–52.

Gad-el-Hak, M. & Blackwelder, R. F. 1985 The discrete vortices from a delta wing. *AIAA J.* **23**, 961–962.

Gad-el-Hak, M. & Blackwelder, R. F. 1986 Control of the discrete vortices from a delta wing. *AIAA J.* **25**, 1042–1049.

Gordnier, R. E. & Visbal, M. R. 1994 Unsteady vortex structure over a delta wing. *J. Aircraft* **31**, 243–248.

Gordnier, R. E. & Visbal, M. R. 1995 Instabilities in the shear layer of delta wings. *AIAA Paper* 95–2281.

Gregory, N., Stuart, J. T. & Walker, W. S. 1955 On the stability of three-dimensional boundary layers with application to the flow due to a rotating disk. *Phil. Trans. R. Soc. Lond.* A **248**, 155–199.

Koumoutsakos, P. & Shiels, D. 1996 Simulations of the viscous flow normal to an impulsively started and uniformly accelerated flat plate. *J. Fluid Mech.* **328**, 177–227.

Lin, C. C. 1945 On the stability of two-dimensional parallel flows. Part II - Stability in an inviscid fluid. *Q. Appl. Maths* **3**, 218–234.

Liou, W. W. 1994 Linear instability of curved free shear layers. *Phys. Fluids* **6**, 541–547.

Lowson, M. V. 1988 The three dimensional vortex sheet structure on delta wings. *AGARD CP* 438, Paper 11.

Lowson, M. V. 1991 Visualisation measurements of vortex flows. *J. Aircraft* **28**, 320–327.

Lowson, M. V., Riley, A. J. & Swales, C. 1995 Flow structure over delta wings. *AIAA Paper* 95–0586.

Murman, E. M. & Rizzi, A. 1986 Applications of Euler equations to sharp edge delta wings with leading edge vortices. *AGARD CP* 412, Paper 15.

Payne, F. M. 1987 The structure of leading edge vortex flows including vortex breakdown. PhD dissertation, University of Notre Dame, USA.

Payne, F. M., Ng, T. T., Nelson, R. C. & Schiff, L. B. 1988 Visualisation and wake surveys of vortical flow over a delta wing. *AIAA J.* **26**, 137–143.

PIERCE, D. 1961 Photographic evidence of the formation and growth of vorticity behind plates accelerated from rest in still air. *J. Fluid Mech.* **11**, 460–464.

POLL, D. I. A. 1985 Some observations of the transition process on the windward face of a long yawed cylinder. *J. Fluid Mech.* **150**, 329–356.

RAYLEIGH, LORD 1880 On the stability, or instability, of certain fluid motions. *Proc. Lond. Math. Soc.* **11**, 57–70. Reproduced in *Scientific Papers* **1**, 474–487. Cambridge University Press.

RAYLEIGH, LORD 1916 On the dynamics of revolving fluids. *Proc. R. Soc. Lond.* A **93**, 148–154. Reproduced in *Scientific Papers* **6**, 447–453. Cambridge University Press.

REYNOLDS, G. A. & ABTAHI, A. A. 1989 Three-dimensional vortex development, breakdown, and control. *AIAA Paper* 89–0998.

RICKARDS, J., SWALES, C. & BARRETT, R. V. 1995 Evaluation of a velocity transformation matrix for three-component LDAs by determining either their beam vectors or by using the motion of the traverse mechanism to provide suitable reference velocities. *Department of Aerospace Engineering Rep.* 712. University of Bristol, UK.

RILEY, A. J. 1996 Vortical flows over delta wings. PhD thesis, University of Bristol, UK.

SARIC, W. S. & REED, H. L. 1988 Stability and transition of three-dimensional boundary layers. *AGARD CP* 438, Paper 1.

SWALES, C., RICKARDS, J., BRAKE, C. J. & BARRETT, R. V. 1993 Development of a pin-hole meter for aligning three dimensional laser Doppler anemometers. *Dantec Information* No. 12, pp. 2–5.

THOMPSON, D. H. 1997 Effect of the leading-edge extension (LEX) fence on the vortex structure over the F/A-18. *Aero. And Maritime Res. Lab. Tech. Rep.* DSTO-TR-0489.

VERHAAGEN, N. G., JENKINS, L. N., KERN, S. B. & WASHBURN, A. E. 1995 A study of the vortex flow over a 76/40-deg double-delta wing. *AIAA Paper* 95–0650.

VERHAAGEN, N. G., MEEDER, J. P. & VERHELST, J. M. 1993 Boundary layer effects on the flow of a leading edge vortex. *AIAA Paper* 93–3463.

VISBAL, M. R. 1995 Computational and physical aspects of vortex breakdown on delta wings. *AIAA Paper* 95–0585.

WASHBURN, A. E. & VISSER, K. D. 1994 Evolution of the vortical structures in the shear layer of delta wings. *AIAA Paper* 94–2317.

WINANT, C. D. & BROWAND, F. K. 1974 Vortex pairing: the mechanism of turbulent mixing-layer growth at moderate Reynolds number. *J. Fluid Mech.* **63**, 237–255.